

## SHIPS PASSING IN THE NIGHT: SPECTROSCOPIC ANALYSIS OF TWO ULTRA-FAINT SATELLITES IN THE CONSTELLATION CARINA <sup>\*†‡</sup>

T. S. LI<sup>1,2</sup>, J. D. SIMON<sup>3</sup>, A. B. PACE<sup>4,29</sup>, G. TORREALBA<sup>5</sup>, K. KUEHN<sup>6</sup>, A. DRLICA-WAGNER<sup>1</sup>, K. BECHTOL<sup>7</sup>, A. K. VIVAS<sup>8</sup>, R. P. VAN DER MAREL<sup>9,10</sup>, M. WOOD<sup>11,12,13</sup>, B. YANNY<sup>1</sup>, V. BELOKUROV<sup>14</sup>, P. JETHWA<sup>15</sup>, D. B. ZUCKER<sup>16,17</sup>, G. LEWIS<sup>18</sup>, R. KRON<sup>1,19</sup>, D. L. NIDEVER<sup>20</sup>, M. A. SÁNCHEZ-CONDE<sup>21,22</sup>, A. P. JI<sup>3,30</sup>, B. C. CONN<sup>23</sup>, D. J. JAMES<sup>24</sup>, N. F. MARTIN<sup>25,26</sup>, D. MARTINEZ-DELGADO<sup>27</sup>, N. E. D. NOËL<sup>28</sup>

(MAGLITES COLLABORATION)

<sup>1</sup> Fermi National Accelerator Laboratory, P.O. Box 500, Batavia, IL 60510, USA

<sup>2</sup> Kavli Institute for Cosmological Physics, University of Chicago, Chicago, IL 60637, USA

<sup>3</sup> Observatories of the Carnegie Institution for Science, 813 Santa Barbara St., Pasadena, CA 91101, USA

<sup>4</sup> George P. and Cynthia Woods Mitchell Institute for Fundamental Physics and Astronomy, and Department of Physics and Astronomy, Texas A&M University, College Station, TX 77843, USA

<sup>5</sup> Institute of Astronomy and Astrophysics, Academia Sinica, P.O. Box 23-141, Taipei 10617, Taiwan

<sup>6</sup> Australian Astronomical Observatory, North Ryde, NSW 2113, Australia

<sup>7</sup> Large Synoptic Survey Telescope, 950 North Cherry Avenue, Tucson, AZ 85721, USA

<sup>8</sup> Cerro Tololo Inter-American Observatory, National Optical Astronomy Observatory, Casilla 603, La Serena, Chile

<sup>9</sup> Space Telescope Science Institute, 3700 San Martin Drive, Baltimore, MD 21218, USA

<sup>10</sup> Center for Astrophysical Sciences, Department of Physics & Astronomy, Johns Hopkins University, Baltimore, MD 21218, USA

<sup>11</sup> Kavli Institute for Particle Astrophysics & Cosmology, P.O. Box 2450, Stanford University, Stanford, CA 94305, USA

<sup>12</sup> SLAC National Accelerator Laboratory, Menlo Park, CA 94025, USA

<sup>13</sup> Department of Physics, Stanford University, 382 Via Pueblo Mall, Stanford, CA 94305, USA

<sup>14</sup> Institute of Astronomy, University of Cambridge, Madingley Road, Cambridge CB3 0HA, UK

<sup>15</sup> European Southern Observatory, Karl-Schwarzschild-Str. 2, 85748 Garching, Germany

<sup>16</sup> Department of Physics & Astronomy, Macquarie University, Sydney, NSW 2109, Australia

<sup>17</sup> Australian Astronomical Observatory, 105 Delhi Rd, North Ryde, NSW 2113, Australia

<sup>18</sup> Sydney Institute for Astronomy, School of Physics, A28, The University of Sydney, NSW 2006, Australia

<sup>19</sup> Department of Astronomy and Astrophysics, University of Chicago, Chicago, IL 60637, USA

<sup>20</sup> National Optical Astronomy Observatory, 950 N. Cherry Ave., Tucson, AZ 85719, USA

<sup>21</sup> Instituto de Física Teórica UAM/CSIC, Universidad Autónoma de Madrid, E-28049 Madrid, Spain

<sup>22</sup> Departamento de Física Teórica, M-15, Universidad Autónoma de Madrid, E-28049 Madrid, Spain

<sup>23</sup> Research School of Astronomy & Astrophysics, Mount Stromlo Observatory, Cotter Road, Weston Creek, ACT 2611, Australia

<sup>24</sup> Event Horizon Telescope, Harvard-Smithsonian Center for Astrophysics, 60 Garden Street, Cambridge, MA 02138, USA

<sup>25</sup> Université de Strasbourg, CNRS, Observatoire astronomique de Strasbourg, UMR 7550, F-67000 Strasbourg, France

<sup>26</sup> Max-Planck-Institut für Astronomie, Königstuhl 17, D-69117 Heidelberg, Germany

<sup>27</sup> Astronomisches Rechen-Institut, Zentrum für Astronomie der Universität Heidelberg, Mönchhofstr. 12-14, 69120 Heidelberg, Germany

<sup>28</sup> Department of Physics, University of Surrey, Guildford, GU2 7XH, UK

Draft version February 21, 2018

### ABSTRACT

We present Magellan/IMACS, Anglo-Australian Telescope/AAOmega+2dF, and Very Large Telescope/GIRAFFE+FLAMES spectroscopy of the Carina II (Car II) & Carina III (Car III) dwarf galaxy candidates, recently discovered in the Magellanic Satellites Survey (MagLiteS). We identify 18 member stars in Car II, including 2 binaries with variable radial velocities and 2 RR Lyrae stars. The other 14 members have a mean heliocentric velocity  $v_{\text{hel}} = 477.2 \pm 1.2 \text{ km s}^{-1}$  and a velocity dispersion of  $\sigma_v = 3.4^{+1.2}_{-0.8} \text{ km s}^{-1}$ . Assuming Car II is in dynamical equilibrium, we derive a total mass within the half-light radius of  $1.0^{+0.8}_{-0.4} \times 10^6 M_{\odot}$ , indicating a mass-to-light ratio of  $369^{+309}_{-161} M_{\odot}/L_{\odot}$ . From equivalent width measurements of the calcium triplet lines of 9 RGB stars, we derive a mean metallicity of  $[\text{Fe}/\text{H}] = -2.44 \pm 0.09$  with dispersion  $\sigma_{[\text{Fe}/\text{H}]} = 0.22^{+0.10}_{-0.07}$ . Considering both the kinematic and chemical properties, we conclude that Car II is a dark-matter-dominated dwarf galaxy. For Car III, we identify 4 member stars, from which we calculate a systemic velocity of  $v_{\text{hel}} = 284.6^{+3.4}_{-3.1} \text{ km s}^{-1}$ . The brightest RGB member of Car III has a metallicity of  $[\text{Fe}/\text{H}] = -1.97 \pm 0.12$ . Due to the small size of the Car III spectroscopic sample, we cannot conclusively determine its nature. Although these two systems have the smallest known physical separation ( $\Delta d \sim 10 \text{ kpc}$ ) among Local Group satellites, the large difference in their systemic velocities,  $\sim 200 \text{ km s}^{-1}$ , indicates that they are unlikely to be a bound pair. One or both systems are likely associated with the Large Magellanic Cloud (LMC), and may remain LMC satellites today. No statistically significant excess of  $\gamma$ -ray emission is found at the locations of Car II and Car III in eight years of *Fermi*-LAT data.

**Keywords:** dark matter; galaxies: dwarf; galaxies: individual (Carina II, Carina III); galaxies: stellar content; Local Group; stars: abundances

## 1. INTRODUCTION

The standard cosmological model with cold dark matter predicts that structure forms hierarchically over a wide range of size scales. The two most prominent satellites of the Milky Way, the Large and Small Magellanic Clouds (LMC and SMC), are both sufficiently massive to expect that they hosted their own populations of luminous satellites prior to their arrival at the Milky Way (D’Onghia & Lake 2008; Sales et al. 2011; Dooley et al. 2017). Indeed, the spatial distribution of the newly discovered ultra-faint dwarf galaxies in the Dark Energy Survey (DES; Abbott et al. 2005) is heavily biased toward the direction of the LMC and SMC, providing strong but indirect observational evidence for the existence of “satellites of satellites” around our Milky Way (Koposov et al. 2015; Bechtol et al. 2015; Drlica-Wagner et al. 2015a; Deason et al. 2015; Jethwa et al. 2016; Sales et al. 2017). Motivated by this distinct anisotropy in the southern satellite distribution, the Magellanic Satellites Survey (MagLiteS) is imaging the unexplored area on the other side of the Magellanic Clouds with the Dark Energy Camera (DECam; Flaugher et al. 2015) on the Blanco 4m telescope at Cerro Tololo Inter-American Observatory. MagLiteS is described in more detail by Drlica-Wagner et al. (2016).

Recently, a pair of dwarf galaxy candidates located on the outskirts of the LMC were discovered using photometric data from MagLiteS: Carina II (Car II) and Carina III (Car III) (Torrealba et al. 2018, hereafter Paper I). These two systems are both extremely faint and close to us, with absolute magnitudes of  $M_V \sim -4.5$  and  $M_V \sim -2.4$ , and heliocentric distances of  $d \sim 37$  kpc and  $d \sim 28$  kpc, respectively. Car II ( $r_{1/2} \sim 90$  pc) is significantly more extended than Car III ( $r_{1/2} \sim 30$  pc). Remarkably, these two objects form a close pair both on the sky (where they have a projected separation of  $18'$  or  $\sim 150$  pc) and along the line of sight (where they are  $\sim 10$  kpc apart), raising the question of whether Car II and Car III are gravitationally bound. Furthermore, due to the proximity of both systems to the LMC ( $\sim 20$  kpc), it seems likely that one or both are (or were) physically associated with the Magellanic Clouds. Kinematic information, such as line-of-sight velocities, is necessary to address these hypotheses, and confirm the nature of the two systems.

Soon after the initial discovery in 2016 December, we began a spectroscopic follow-up program with the Magellan Baade Telescope, the Anglo-Australian Telescope (AAT), and the Very Large Telescope (VLT). Rapid follow-up with the AAT and VLT was possible thanks to short turn-around time for approval of service observations and Director’s Discretionary time. Our multi-pronged observational strategy enabled both deep observations of a smaller number of faint targets with the 8-m-class Magellan and VLT, and wider-field observations

of a large number of brighter targets (in both Car II and Car III together) with the AAT.

Here, we report the first spectroscopic analysis of the Car II and Car III dwarf galaxy candidates discovered in MagLiteS. In §2, we describe the observations with all three telescopes, and the data reduction procedures. In §3, we detail the results from our spectroscopic program, including the set of spectroscopic members, and measurements of the radial velocity, velocity dispersion, mean metallicity, and metallicity dispersion for each dwarf galaxy candidate. In §4, we discuss the implications of these derived parameters as they relate to the classification of Car II and Car III, along with other unique features of this pair – specifically, the possible tidal interaction between the two systems, and the association of Car II and Car III with the Magellanic Clouds. We also briefly discuss the search for dark matter annihilation within the Carina systems. We conclude in §5.

The photometry in this work has been dereddened using the Schlegel et al. (1998) extinction map around Car II and Car III. Because of the relatively low Galactic latitude, the average reddening in this region is  $E(B - V) \sim 0.19$ .

## 2. OBSERVATIONS AND DATA REDUCTION

2.1. *Magellan/IMACS Spectra*

We obtained multi-slit spectroscopy of Car II and Car III with the IMACS spectrograph (Dressler et al. 2006) on the Magellan Baade telescope on 2017 January 24–25. The observing setup was the same as for the spectroscopy of the Tucana III (Simon et al. 2017) and Eridanus II (Li et al. 2017) dwarf galaxies. We used the f/4 camera on IMACS, which provides a full field-of-view of  $15.4' \times 15.4'$ . The spectrograph was configured with the 1200  $\ell/\text{mm}$  grating and a tilt angle of  $32.4^\circ$ , producing a spectral resolution of  $R \sim 11,000$  for a  $0''.7$  slit width and a wavelength range of at least  $7550 - 8750 \text{ \AA}$  for each slit. This wavelength range covers the calcium triplet (CaT) lines around  $8500 \text{ \AA}$ , used for measuring radial velocities and metallicities of candidate member stars, as well as the telluric absorption lines (Fraunhofer A-band) around  $7600 \text{ \AA}$  used for the correction of velocity errors caused by mis-centering of the stars within the slits (see Sohn et al. 2007 for details).

The target selection and mask design for Magellan/IMACS (hereafter IMACS) were performed using the photometry from the original MagLiteS catalog. Based on the knowledge of confirmed members of the DES-discovered dwarf galaxies Reticulum II from Simon et al. (2015) and Tucana III from Simon et al. (2017), we used similar selection criteria as described in Simon et al. (2017). Target selection and mask design used a preliminary estimate for the distance modulus for Car II (Car III) of  $m - M = 17.5$  ( $m - M = 17.1$ ). For Car II, the red giant branch (RGB) candidate members were selected to be redder than the fiducial sequence of the metal-poor globular cluster M92 from An et al. (2008), bluer than a 12 Gyr,  $[\text{Fe}/\text{H}] = -2.2$  theoretical PARSEC isochrone<sup>31</sup> from Bressan et al. (2012), and

tingli@fnal.gov

\* This paper includes data gathered with the 6.5-meter Magellan Telescopes located at Las Campanas Observatory, Chile.

† This paper includes data gathered with Anglo-Australian Telescope in Australia.

‡ Based on data products from observations made with ESO Telescopes at the La Silla Paranal Observatory under programme ID 298.B-5027.

<sup>31</sup> Note that an earlier version of the PARSEC isochrone was used. See the Appendix for more details regarding the updated PARSEC isochrones.

**Table 1**  
Observations

Mask/Run name	$\alpha$ (J2000) (h m s)	$\delta$ (J2000) ( $^{\circ}$ ' ")	Slit PA (deg)	$\lambda/\Delta\lambda$	disp. $\text{\AA}/\text{pix}$	# of exp	$\Sigma t_{\text{exp}}$ (sec)	seeing (")	MJD <sup>a</sup>	# of slits/fibers	# of useful spectra
IMACS-Car2Mask1	07:36:36.00	-57:57:20.0	172.0	11,000	0.19	2	4500	1''2	57779.3	72	32
IMACS-Car2Mask2	07:36:26.00	-58:02:00.0	248.0	11,000	0.19	3	6000	1''5	57778.3	48	33
IMACS-Car3Mask1	07:38:28.00	-57:53:30.0	317.0	11,000	0.19	6	13200	2''5	57778.2	67	40
IMACS-Car3LongSlit	07:38:34.84	-57:52:11.2	180.0	11,000	0.19	1	1800	1''2	57779.3	1	1
AAT-Jan	07:36:33.60	-58:01:12.0	-	10,000	0.24	5	13200	1''3	57777.6	388	131
AAT-May	07:36:33.60	-58:01:12.0	-	10,000	0.24	2	4800	2''0	57902.4	309	55
VLT-Feb	07:37:32.40	-57:57:16.0	-	6,000	0.20	1	2775	0''3	57811.1	116	116

<sup>a</sup> The date listed here is the weighted mean observation date over multiple exposures. For AAT-Jan observations, the date is the weighted mean over multiple nights.

brighter than  $g = 20.8$ . Several candidate blue horizontal branch (BHB) stars were selected at  $17.7 < g < 18.8$  and  $g - r < 0.1$ ; a handful of candidate red horizontal branch (RHB) stars were selected at  $17.9 < g < 18.6$  and  $0.1 < g - r < 0.3$ . Potential main sequence turnoff (MSTO) stars were selected using a 0.1 mag wide window in  $g - r$  around the PARSEC isochrone for  $20.8 < g < 22$  (although because of the observing conditions, we did not get any useful spectra for MSTO candidates).

For Car III, we used the same selection criteria as for Car II, with the exception of shifting all sequences 0.4 mag brighter according to the difference in distance moduli. Based on these targets, we designed two slit-masks (IMACS-Car2Mask1 and IMACS-Car2Mask2) near the center of Car II and one slitmask (IMACS-Car3Mask1) near the center of Car III, using the `maskgen` program<sup>32</sup>. Stars were placed on the slit masks in a category prioritization descending order of BHB, RGB, RHB and MSTO. Within each category, priorities were based on brightness and distance from the center of Car II or Car III. Finally, any remaining mask space was filled by stars with photometry that made them unlikely to be members. IMACS-Car2Mask1 contains 72 slits, IMACS-Car2Mask2 contains 48 slits and IMACS-Car3Mask1 contains 67 slits. All the targets, observed with IMACS and other instruments described in later sections, are presented in Figure 1.

We obtained a 1.7-hr exposure with IMACS-Car2Mask2 and 3.7-hr exposure with IMACS-Car3Mask1 on 2017 January 24, and 1.25-hr exposure on IMACS-Car2Mask1 on 2017 January 25. One of the BHB candidates, MAGLITES J073834.84-575211.2, on IMACS-Car3Mask1 happened to fall in a gap between CCDs, so we also obtained a 30-min exposure on this star with a 0''7-wide long slit (IMACS-Car3LongSlit) on 2017 January 25. The observing conditions on both nights were relatively poor, with high humidity and  $\sim 1'' - 3''$  seeing.

We reduced the IMACS spectra following the procedures described by Simon et al. (2017) for Tucana III. We first performed the bias subtraction and removal of read-out pattern noise, then we used the Cosmos pipeline (Dressler et al. 2011; Oemler et al. 2017) to derive an initial wavelength solution and performed the slit mapping, followed by a refined wavelength calibration and spectral extraction using an IMACS pipeline derived from the DEEP2 data reduction pipeline for

Keck/DEIMOS (Cooper et al. 2012). For each mask, the extracted spectra from multiple exposures were combined using inverse-variance weighting. The combined spectra reach a signal-to-noise ratio (S/N)  $\sim 5 \text{ pixel}^{-1}$  at  $r = 19.0$  for Car II and at  $r = 19.3$  for Car III.

The details of the instrument setup, observing information, mask information, etc., for IMACS and other instruments described in later sections, are summarized in Table 1.

## 2.2. AAT/AAOmega+2dF Spectra

We observed Car II and Car III with the AAOmega Spectrograph (Sharp et al. 2006), a fiber-fed multi-object spectrograph on the 3.9 m Anglo-Australian Telescope (AAT) at Australian Astronomical Observatory (AAO). The AAOmega Spectrograph is fed by the Two Degree Field (“2dF”) multi-object system, allowing acquisition of up to 392 simultaneous spectra of objects within a  $2^{\circ}$  field on the sky.

AAOmega is a dual-beam spectrograph, which feeds a blue arm and a red arm with a beam splitter at 5700  $\text{\AA}$ . For the red arm, we utilized the 1700D grating, providing a spectral resolution of  $R = 10,000$  and wavelength coverage of 8400 – 8810  $\text{\AA}$ , which enables us to target the spectral region of the CaT absorption lines for velocity and metallicity measurements. For the blue arm, we chose the 580V grating with resolution of  $R = 1,300$  and wavelength coverage of 3750 – 5750  $\text{\AA}$ , which allows us to study additional elements (e.g., carbon) in the blue. This paper focuses on the kinematics and metallicities of the Carina systems, and therefore the spectra from the blue arm will be discussed in a future paper.

Observations with AAT/AAOmega+2dF (hereafter AAT) were taken on 2017 January 23 and May 29 through the service observing program, and on 2017 January 25 through classical observing time. We obtained three 40-min exposures on January 23, one 40-min exposure and one 60-min exposure on January 25, and two 40-min exposures on May 29. To ensure accurate velocity determination, the arc frames were taken right before the science exposures at the same position. During the January run, the seeing was around  $1''-1''5$  with intermittent clouds. During the May run, the weather was clear with seeing around  $1''6-2''2$ . Among the 392 fibers, 25 of them were assigned to sky positions, 8 of them were assigned to guide stars selected from the UCAC4 catalog (Zacharias et al. 2013), and the remaining fibers were assigned to target stars.

The targets for the AAT run were mostly selected us-

<sup>32</sup> <http://code.obs.carnegiescience.edu/maskgen>

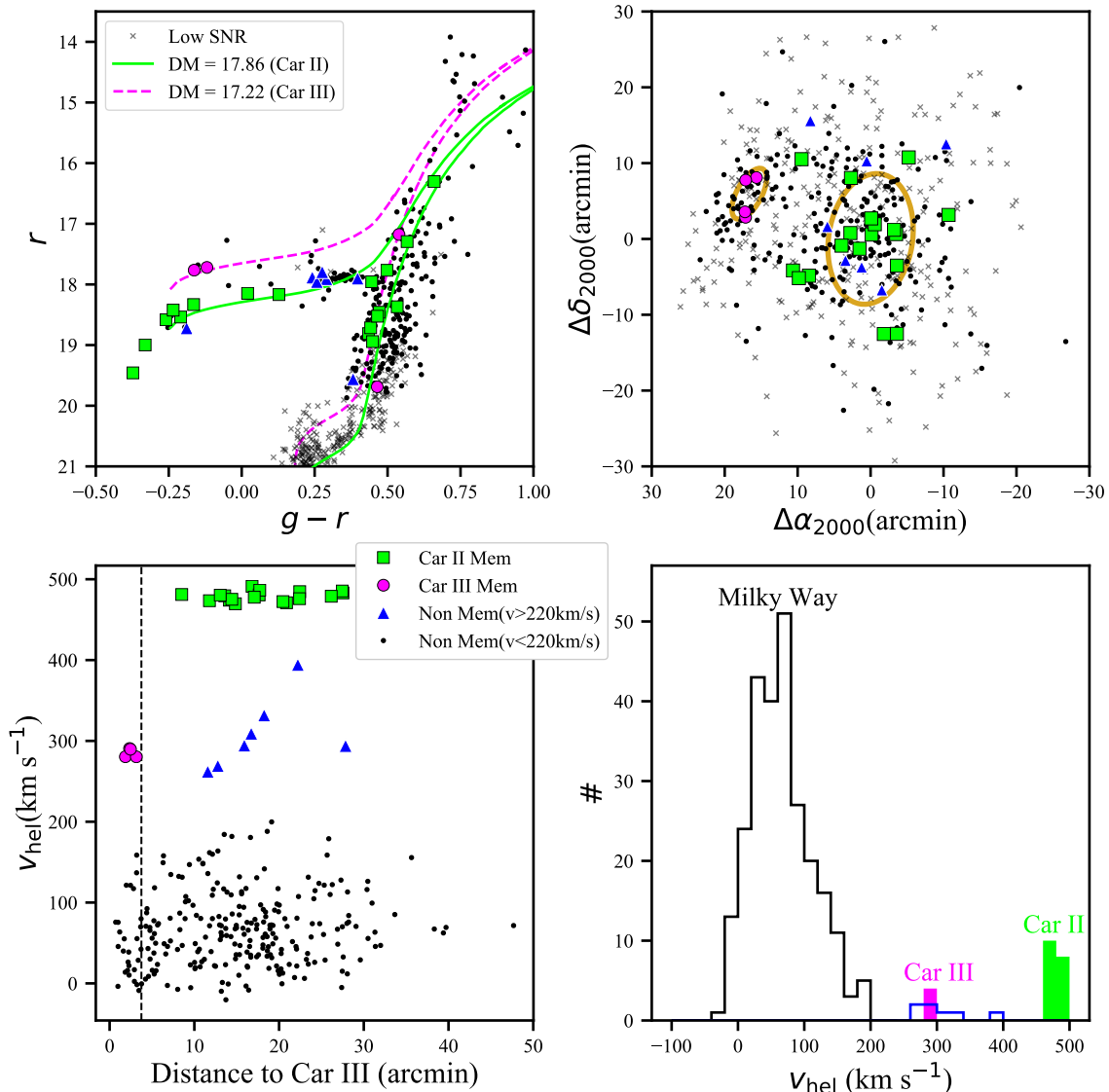


**Figure 1.** *upper-left:* Color-magnitude diagram for observed stars with Magellan/IMACS, AAT/2dF+AAOmega and VLT/GIRAFFE+FLAMES. Overplotted are the PARSEC isochrones of a metal-poor population with age = 12.0 Gyr,  $[\text{Fe}/\text{H}] = -2.2$  at the distance of Car II ( $m - M = 17.86$ , green) and Car III ( $m - M = 17.22$ , magenta). Green squares indicate 18 members of Car II, magenta circles indicate 4 members of Car III, blue triangles indicate 7 non-members with velocities  $v_{hel} > 220 \text{ km s}^{-1}$ , and small black dots are remaining non-member with velocities  $v_{hel} < 220 \text{ km s}^{-1}$ ; black cross markers indicate candidate members that were observed but for which we were unable to obtain velocity measurements (mainly due to low S/N). *upper-right:* Spatial distribution of the targets. Gold ellipses show the half-light radius of Car II (larger ellipse) and Car III (smaller ellipse). *lower-left:* Heliocentric velocity versus distance from the center of Car III. The separation between the Car II members, Car III members and the non-members is obvious. A few non-members have velocities similar to that of Car III, but are far away from the Car III center. The black dashed line indicates the half-light radius of Car III ( $r_h = 3.75'$ ; Paper I). *lower-right:* Velocity distribution of 283 stars with successful velocity measurements. Car II members are indicated as the peak around  $480 \text{ km s}^{-1}$  (in green) and Car III members are indicated as the peak around  $280 \text{ km s}^{-1}$  (in magenta). A few stars have velocities close to Car III and are shown as a blue histogram. From their position on the sky (upper-right panel) and their distance from Car III (lower-left panel) we conclude that they are not members of Car III.

ing the photometry from the original MagLiteS catalog. The RGB and RHB candidates were selected using the best-fit PARSEC isochrone for Car II (log age = 10.0,  $[\text{Fe}/\text{H}] = -1.7$ ,  $m - M = 17.5$ ) and Car III (log age = 9.75,  $[\text{Fe}/\text{H}] = -0.9$ ,  $m - M = 17.1$ ) at the time of the observations<sup>33</sup>. The BHB candidates were selected us-

ing a fiducial M92 BHB isochrone placed at the distance modulus of Car II and Car III.

In addition to MagLiteS photometry, we also used photometry from time-series follow-up observations (to search for RR Lyrae stars) acquired with DECam during Blanco 4-m Director's Discretionary and engineering time. The exposure times for these follow-up studies were shorter than the original MagLiteS exposures and therefore brighter stars could be observed. In addition,  $u$ -band measurements were performed in the follow-up observations, and a handful of K/M giant candidates

<sup>33</sup> Note that the final isochrone parameter values reported in Paper I are different from those used for spectroscopic target selection because the photometry and the fits continued to be refined after the spectroscopic observations were obtained.

were selected based on the  $u - g$  and  $g - i$  color (e.g., see Figure 2 of Yanny et al. 2009). Furthermore, we included some RR Lyrae candidates from the preliminary analysis of time-series follow-up studies. Thanks to the proximity of Car II and Car III on the sky, as well as the large field of view of AAT+2dF, both systems were targeted in a single pointing. We assigned RR Lyrae candidates the highest priority, followed by the BHB and K/M giant candidates. Stars in two remaining categories (RGB, RHB) were prioritized based on their brightness in  $r$ -band. Note that the target spacing of 2dF is typically  $30'' - 40''$  due to fiber collisions, and therefore some targets located close to the centers of Car II and Car III were missed where the target density is high.

The candidate stars were then allocated according to the priorities described above using the fiber configuration program `configure`<sup>34</sup> provided by AAO. Flexibility in target allocation with 2dF allowed us to identify bright ( $S/N > 20$  per pixel) non-member stars in the January 23 data, leading to re-allocation of those fibers to alternate targets during the January 25 observations. 388 candidates were targeted in total from the two nights of observations in the January run; 309 of them were targeted again in the May run.

The data reduction was performed using the `2dfdr`<sup>35</sup> v6.28 data reduction program of the AAO. The reduction includes bias subtraction, scattered light subtraction, flat-fielding, optimal spectral extraction, wavelength calibration, sky subtraction, and frame combination with cosmic ray rejection. Wavelength calibration was first performed using the arc frames taken immediately before or after each science exposure, followed by a recalibration with a second order polynomial fit using sky emission lines. As the observations were taken from different nights, the reduced spectra were corrected for the heliocentric motion of the Sun at each exposure, before the spectra from multiple exposures were combined using inverse-variance weighting. To detect possible binary stars, we combined the spectra from the January run (AAT-Jan) and May run (AAT-May) separately for the velocity measurements. The combined spectra have  $S/N \sim 5 \text{ pixel}^{-1}$  at  $r = 18.7$  for AAT-Jan and at  $r = 18.0$  for AAT-May.

### 2.3. VLT/GIRAFFE+FLAMES Spectra

After the observations with AAT and Magellan, we also observed Car II and Car III with the GIRAFFE+FLAMES spectrograph (Pasquini et al. 2000) on the 8.2-m Kueyen telescope (UT2) based at the ESO-VLT through Director's Discretionary Time. Observations were taken in MEDUSA mode, which allows the simultaneous observation of up to 132 objects, with a minimum target separation of  $11''$  due to fiber collisions. On the night of 2017 February 26, one 2775-second exposure was taken under excellent seeing condition ( $\sim 0''.3$ ). The LR8 grating was used for this observation, which covers the wavelength range from 8206 – 9400 Å at a resolution of  $R \sim 6,000$ . The calibration frames, including biases, flats and ThAr arcs, were taken at the end of the night.

Target selection for VLT/GIRAFFE+FLAMES (hereafter VLT) was done in a similar way as for the AAT, with the exception that we manually shifted the best-fit PARSEC isochrone  $g - r \sim 0.07$  bluer, based on the confirmed Car II members identified by IMACS and AAT<sup>36</sup>. As the field of view of FLAMES is about  $25'$  in diameter, we centered the exposure field in between Car II and Car III and we therefore missed some of the BHB members found in the AAT data (see §3). 116 targets were selected to feed to FLAMES, with 13 fibers assigned to blank sky positions.

As only a single exposure was obtained with VLT, we first removed cosmic rays using L.A.Cosmic (van Dokkum 2001). We then reduced the data with the GIRAFFE `Gasgano` pipeline (v2.4.8) provided by ESO for bias subtraction, flat-fielding, wavelength calibration and spectral extraction of individual objects. We performed a wavelength re-calibration using sky emission lines and a sky subtraction with our own code. For details, we refer to the spectroscopic analysis of the Horologium I dwarf galaxy (Li et al., in prep.). In summary, a first-order wavelength correction derived from sky lines was applied to every spectrum to compensate for the wavelength shift likely caused by the temperature changes between the science observing during the night and the calibration frames taken at the end of the night. We then combined the 13 sky fibers into a master sky spectrum. To compensate for fiber-to-fiber throughput and resolution variations, for each target spectrum we degraded the resolution of either the target spectrum or the master sky spectrum (whichever had the higher resolution) and then scaled the master sky spectrum to match the intensity of the sky lines in the target spectrum before the subtraction. The final reduced spectra (referred to as VLT-Feb) have  $S/N \sim 7 \text{ pixel}^{-1}$  at  $r \sim 19.8$ .

## 3. RESULTS

In this section, we present the results derived from the observations taken from three telescopes. We first determine the radial velocity of each individual candidate star. We then identify member stars based on the velocity, spatial location, and location on the color-magnitude diagram. After identifying the member stars, we also compute the systemic velocity, velocity dispersion, mean metallicity and metallicity dispersion for Car II and Car III.

We use the distance moduli (dereddened) and structural parameters from Paper I for the analysis in this work, unless otherwise stated. These parameters, together with the derived quantities in this section, are summarized in Table 2. We note that for Car II, the distance modulus derived from RR Lyrae in Paper I has smaller uncertainties and is used in this work.

### 3.1. Radial Velocity Measurements

The reduced spectra from IMACS, AAT, and VLT were used for radial velocity measurements following the method described in Li et al. (2017). We measured the heliocentric radial velocities ( $v_{\text{hel}}$ ) by fitting the reduced spectra with velocity templates using a Markov chain

<sup>34</sup> <https://www.aao.gov.au/science/software/configure>

<sup>35</sup> <https://www.aao.gov.au/science/software/2dfdr>

<sup>36</sup> The original PARSEC synthetic isochrones used an out-of-date DECcam system response. See details about this shift in the Appendix.

**Table 2**  
Summary of Properties of Carina II and Carina III<sup>a</sup>

Row	Property	Carina II	Carina III
(1)	RA (J2000)	114.1066 ± 0.0070	114.6298 ± 0.0060
(2)	Dec (J2000)	-57.9991 ± 0.0100	-57.8997 ± 0.0080
(3)	( $m - M$ )	17.86 ± 0.02 <sup>b</sup>	17.22 ± 0.10
(4)	Heliocentric Distance (kpc)	37.4 ± 0.4 <sup>b</sup>	27.8 ± 0.6
(5)	$M_{V,0}$	-4.5 ± 0.1	-2.4 ± 0.2
(6)	$L_{V,0}$ ( $L_{\odot}$ )	5.4 ± 0.5 × 10 <sup>3</sup>	7.8 <sup>+1.6</sup> <sub>-1.3</sub> × 10 <sup>2</sup>
(7)	$r_{1/2}$ (arcmin)	8.69 ± 0.75	3.75 ± 1.00
(8)	$r_{1/2}$ (pc)	91 ± 8	30 ± 9
(9)	$\epsilon = 1 - b/a$	0.34 ± 0.07	0.55 ± 0.18
(10)	PA (N to E; deg)	170 ± 9	150 ± 14
(11)	Number of Members	14 <sup>c</sup>	4
(12)	$v_{\text{hel}}$ (km s <sup>-1</sup> )	477.2 ± 1.2	284.6 <sup>+3.4</sup> <sub>-3.1</sub>
(13)	$v_{\text{GSR}}$ (km s <sup>-1</sup> )	235	42
(14)	$\sigma_v$ (km s <sup>-1</sup> )	3.4 <sup>+1.2</sup> <sub>-0.8</sub>	5.6 <sup>+4.3</sup> <sub>-2.1</sub> <sup>d</sup>
(15)	$M_{\text{half}}$ ( $M_{\odot}$ )	1.0 <sup>+0.8</sup> <sub>-0.4</sub> × 10 <sup>6</sup>	.....
(16)	$M/L_V$ ( $M_{\odot}/L_{\odot}$ )	369 <sup>+309</sup> <sub>-161</sub>	.....
(17)	$\frac{dv}{dx}$ (km s <sup>-1</sup> arcmin <sup>-1</sup> )	0.0 ± 0.3	.....
(18)	Mean metallicity	-2.44 ± 0.09	-1.97 <sup>e</sup>
(19)	Metallicity dispersion (dex)	0.22 <sup>+0.10</sup> <sub>-0.07</sub>	.....
(20)	$\log_{10} J(0.1^{\circ})$ (GeV <sup>2</sup> cm <sup>-5</sup> )	17.9 <sup>+0.6</sup> <sub>-0.5</sub>	19.9 <sup>+1.0</sup> <sub>-0.9</sub> <sup>d</sup>
(21)	$\log_{10} J(0.5^{\circ})$ (GeV <sup>2</sup> cm <sup>-5</sup> )	18.2 <sup>+0.5</sup> <sub>-0.5</sub>	20.2 <sup>+1.0</sup> <sub>-0.9</sub> <sup>d</sup>
(22)	$\log_{10} D(0.1^{\circ})$ (GeV cm <sup>-2</sup> )	16.9 <sup>+0.3</sup> <sub>-0.3</sub>	17.8 <sup>+0.5</sup> <sub>-0.5</sub> <sup>d</sup>
(23)	$\log_{10} D(0.5^{\circ})$ (GeV cm <sup>-2</sup> )	18.0 <sup>+0.4</sup> <sub>-0.4</sub>	18.8 <sup>+0.6</sup> <sub>-0.7</sub> <sup>d</sup>

**Note.** — (a) Rows (1)–(10) are taken or derived from Paper I. Values in rows (11)–(23) are derived using the measurements in this paper. All values reported here (and in this paper) are from the 50th percentile of the posterior probability distributions. The uncertainties are from the 16th and 84th percentiles of the posterior probability distributions.

(b) The distance derived from RR Lyrae in Paper I is listed here as the heliocentric distance of Car II and is used throughout the paper. For other quantities, parameters derived from CMD fit are used instead.

(c) There are 18 spectroscopic members but only the 14 non-variable stars are used for kinematic analysis.

(d) Note that the velocity dispersion and the J-factor for Car III is calculated based on only four spectroscopic members. We caution the use of this calculation as the classification of Car III is remain unclear.

(e) Note that this is the metallicity of the brightest member in Car III and not the mean metallicity of the system.

Monte Carlo (MCMC) sampler and finding the best-fit velocity that maximizes the likelihood defined by Eq. 1 in Li et al. (2017). Instead of using only one velocity template per spectrum, we defined a set of templates for each instrument and used the template that gave the largest likelihood at the best-fit velocity as the best template for each star. The template set for each instrument includes at least one metal-rich RGB, one metal-poor RGB, and one BHB star. The velocity templates for AAT and IMACS were observed using the same instrument setting as the science observation and were constructed following the description in Simon et al. (2017). We were not able to obtain any velocity template spectra during the VLT run. Instead, we used the Keck/DEIMOS templates from Kirby et al. (2015a), as the Keck/DEIMOS spectra have a much wider wavelength coverage and a similar resolution ( $R \sim 6,000$ ) as our VLT spectra. For the IMACS spectra, we also applied a telluric correction derived using a telluric template to correct for the mis-centering of spectroscopic targets within each slit (see Li et al. 2017 for more details).

The statistical uncertainty on each velocity measurement is calculated as the standard deviation of the poste-

rior velocity distribution from the MCMC sampler. This error is related primarily to the S/N of the spectra, with stellar temperature and metallicity also playing a role. Other systematic effects, such as instrument flexure, uncertainties in the wavelength calibration, uncertainties in the template velocity and template mismatching, should also be considered in the final velocity uncertainty budget. We estimated the systematic uncertainty as the quadrature difference between repeat measurements and the statistical uncertainty (c.f. Simon & Geha 2007; Simon et al. 2017; Li et al. 2017). We adopted the systematic floor of 1.0 km s<sup>-1</sup> for IMACS from Simon et al. (2017). For AAT, we determine the systematic floor to be 0.5 km s<sup>-1</sup> using repeat measurements of 18 bright stars (S/N > 8) from the January run and the May run. Since only one exposure was taken with VLT, we were not able to derive a systematic floor with this dataset. We adopted a systematic floor of 0.9 km s<sup>-1</sup> from the VLT observations of Horologium I (Li et al., in prep), which has the same instrument setup as this data set. We added these systematic uncertainties in quadrature with the statistical uncertainties to obtain the final reported velocity uncertainties  $\delta_v$ .

In order to combine the velocities derived from three different spectrographs to produce the final dataset for the velocity dispersion determination in §3.3, we need to verify that there is no systematic offset between these three data sets. We compare the repeated measurements from different instruments as shown in the top panels Figure 2 and find no obvious systematic offset between any given pair of instruments. In order to confirm that our error estimation is reasonable for each instrument, we again use these repeated measurements from each pair of instruments and compute the distribution of velocity differences between the two independent measurements ( $v_1, v_2$ ), divided by the quadrature sum of their uncertainties ( $\sqrt{\delta_1^2 + \delta_2^2}$ ). The resulting distributions shown in the bottom panels of Figure 2 are well-described by normal distributions with zero mean and unit variance, as shown by red dashed curves in the same plots. From this comparison, we conclude that there is no significant zero-point shift between the various spectrographs, and that combining the three datasets will not introduce additional velocity uncertainties.

In order to study the kinematics of Car II and Car III, as well as the spectroscopic membership in each system, we combined the velocity measurements from the three different instruments into a single data set. With this combined sample, we successfully determined the velocities of 283 stars. The heliocentric velocities and the associated uncertainties are reported in Table 4. We note that although the results reported in the table are from each observing run or each mask, we used the weighted average ( $w = 1/\delta^2$ ) for stars with more than one measurement for the remainder of this paper.

### 3.2. Spectroscopic Membership Determination

Figure 1 shows the color-magnitude diagram (CMD), spatial distribution, and velocity distribution of the observed stars in both systems. We identified a total of 18 members in Car II and 4 members in Car III from the combined sample (see below).

The 18 members in Car II form a coherent velocity peak near  $480 \text{ km s}^{-1}$  in the heliocentric velocity distribution (lower right panel), including 6 BHB members, 2 RR Lyrae members, and 10 RGB members. Since the heliocentric velocity of Car II is quite high relative to the mean velocity and velocity dispersion of the Milky Way halo, there are no foreground contaminants anywhere near the velocity of Car II. Furthermore, all stars within this velocity peak fall on the Car II isochrone, making the membership of this system unambiguous. The BHB members are all far from the center of Car II ( $r > 10'$ ) and therefore 4 of them are only observed with AAT. The velocity uncertainties of these BHB members are relatively large as a result of their broad lines and the low S/N of their spectra. The brightest RGB member, MAGLITES J073621.25–575800.3, was observed both in January (AAT & IMACS) and in May (AAT). The difference between the January and May observations is  $\sim 30 \text{ km s}^{-1}$ . Another RGB member, MAGLITES J073646.47–575910.2, was observed both in January (AAT & IMACS) and February (VLT), and the difference is  $\sim 25 \text{ km s}^{-1}$ . We therefore conclude that these two stars are binaries. The 2 RR Lyrae members of Car II also show velocity variability, and are discussed

in more detail in §3.2.2.

We find a second narrow peak in the velocity distribution, containing 4 stars, centered at  $280 \text{ km s}^{-1}$ . All four stars are located within the Car III half-light radius and we therefore identify them as Car III members. While it is difficult to confirm an association based on only four stars, two of the four are BHB stars at the distance of Car III ( $m - M = 17.22$ , see upper-left panel in Figure 1). The brighter of the two RGB stars lies exactly on the expected Car III isochrone, while the fainter one is slightly redder than expected. Nevertheless, the combination of the spatial coincidence between these stars and their position in the CMD strongly suggests that this group is related to Car III.

Finally, seven candidate stars have velocities in the range of  $260\text{--}400 \text{ km s}^{-1}$  and are displayed in blue in Figure 1. Given their velocities, these stars are clearly not members of Car II. Their CMD positions and large distance away from Car III also indicate that they are not Car III members. We used the Besançon Galactic stellar model (Robin et al. 2003) to estimate the expected number of foreground Milky Way stars in our spectroscopic sample. We selected simulated stars within  $0.2 \text{ mag}$  of the PARSEC isochrone and with  $r < 19.5$ . We found that in an area of  $1 \text{ deg}^2$  centered on Car II there are  $\sim 15$  simulated stars that have a velocity larger than  $260 \text{ km s}^{-1}$ , with a majority at  $g - r < 0.4$  (i.e., foreground main-sequence stars). The surface density of non-Car II and Car III members in our spectroscopic sample is similar to this value. The small number of contaminants from the Besançon model further supports the conclusion that the two peaks are associated with Car II and Car III members. Given that Car II is relatively close to the LMC on the sky, some of these non-member stars might also belong to the LMC, which is discussed further in §3.2.1.

#### 3.2.1. LMC Contamination

The field of Car II and Car III is located  $18^\circ$  ( $\sim 20 \text{ kpc}$ ) from the center of the LMC. While the visible body of the LMC is contained within the central  $\sim 10^\circ$  (e.g., Besla et al. 2016), stars associated with the LMC have been detected as far out as  $\sim 20^\circ$  (e.g., Nidever et al. 2017). Recently, Belokurov & Koposov (2016) also reported the detection of a small number of BHB candidates likely associated with the Magellanic Clouds, at a wide range of angular distances, extending out to  $\sim 30^\circ$  or perhaps even  $\sim 50^\circ$  from the LMC. Interestingly, the diffuse cloud of BHB-like stars appears rather clumpy; the authors identify at least four individual stream-like structures. The most significant of these, the so-called S1 stream, can be traced securely to  $20 - 25^\circ$  from the LMC. Further support for the picture in which the LMC is enshrouded in a thin veil of stellar debris comes from the studies of Mackey et al. (2016) and Belokurov et al. (2017), who use main sequence and RR Lyrae stars, respectively, to trace a halo-like component around the LMC out to  $\sim 20^\circ$  from its center. Finally, as Boubert et al. (2017) demonstrate using a combination of a stellar evolution code and N-body simulations of the LMC in-fall, the Cloud ought to be surrounded by an envelope of runaway stars. These high-velocity escapees are kicked out of the dwarf's disk during stellar binary disruption as a result of core-collapse supernova explosions, and can travel many tens

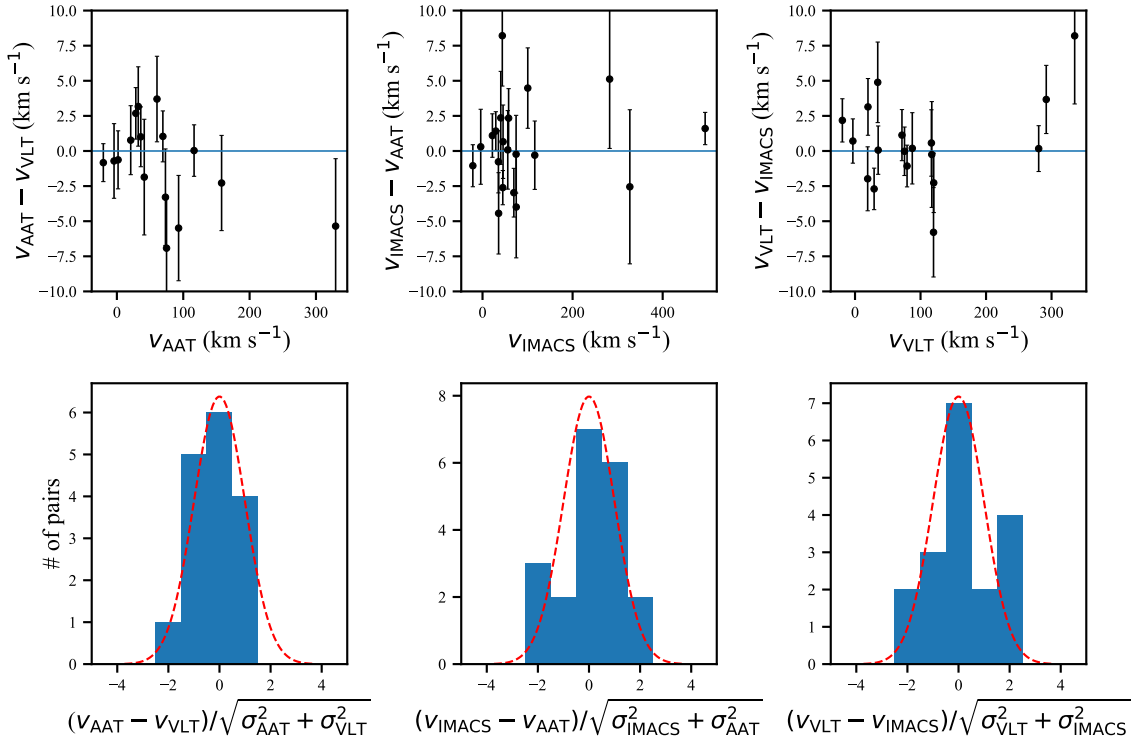


**Figure 2.** *Top Row:* We compare velocity measurements from different instruments using repeated measurements. There are no obvious zero-point shifts between three instruments. *Bottom Row:* Radial velocity uncertainty estimation tests using the repeated observations from different instruments. The histograms show the distributions of the velocity difference normalized by the quadrature sum of their uncertainties. The red dashed curves show a normal distribution with zero mean and unit variance scaled by the total number of pairs. The good agreement with the blue histograms indicates that our estimation of the velocity uncertainties is reasonable.

of kpc away from the LMC in all directions.

It is therefore possible that some stars in our spectroscopic sample belong to the LMC. To calculate what the velocities of such stars might be, we used the rotating disk models of van der Marel & Sahlmann (2016). These imply that the line-of-sight velocity of the LMC disk at the sky position of Car II and Car III is 380 km s<sup>-1</sup>. This is 118 km s<sup>-1</sup> higher than the systemic velocity of the LMC center of mass, due to the fact that far from the center of the galaxy a significant component of its large transverse velocity vector projects along the line of sight. The location of Car II and Car III is on the near side of the inclined LMC disk, so the distance to the disk there is only 43.5 kpc. Since the positions of Car II and Car III are near the kinematic minor axis, a possible non-rotating LMC halo population would have more-or-less the same velocity (namely, 380 km s<sup>-1</sup>) as the rotating disk. Old populations in the visible part of the LMC have velocity dispersions in the range 20–30 km s<sup>-1</sup> (van der Marel et al. 2009). van der Marel et al. (2002) also shows that the velocity dispersion is almost a constant of  $\sim 20$  km s<sup>-1</sup> between 2 kpc and 9 kpc from the LMC center. We expect the dispersion at the position of Car II and Car III ( $\sim 20$  kpc from LMC) to be similar, though it largely depends on the mass and extent of the LMC’s dark halo. Moreover, the tidal radius of the LMC is  $24.0^\circ \pm 5.6^\circ$  (van der Marel & Kallivayalil 2014). Therefore, tidal perturbations could affect both the mean velocity and velocity dispersion of LMC stars at the position of Car II and Car III.

The mean velocities inferred here for Car II and Car III

are offset by  $\sim \pm 100$  km s<sup>-1</sup>, respectively, from the predicted velocities of LMC members. Therefore, contamination by LMC members at the Car II and Car III velocities is expected to be negligible. We do detect 7 non-member stars (triangles in Figure 1; see also Table 4) with  $v_{\text{hel}}$  in the range 260–400 km s<sup>-1</sup>. These velocities correspond to much smaller velocities in the Galactocentric frame ( $\sim 40$ –180 km s<sup>-1</sup>), since Car II and Car III are located almost opposite from the direction of solar motion. Among these 7 stars, 6 have  $0.2 < g - r < 0.4$  and are very likely to be foreground halo stars at much closer distances. The seventh star, MAGLITES J073634.86–580340.6, is a BHB star with  $g - r \sim -0.2$ . From the CMD (see upper-left panel in Figure 1), its distance is slightly farther than that of Car II. Comparing its  $r$ -band magnitude with the BHB members in Car II and Car III, we estimate the distance modulus of this star to be  $m - M = 18.1 \pm 0.1$ , corresponding to a heliocentric distance of  $42 \pm 2$  kpc, matching well with the model prediction of  $\sim 43.5$  kpc for the near side of the LMC mentioned above. This BHB star has independent observations from AAT, IMACS and VLT. The weighted average velocity is  $v_{\text{hel}} = 331.7 \pm 2.0$  km s<sup>-1</sup>, showing no evidence of binary motion. For comparison, Muñoz et al. (2006) detect a group of LMC stars in the field of the Carina dwarf spheroidal galaxy ( $\sim 22^\circ$  from LMC center and  $\sim 10^\circ$  from Car II and Car III) with an average radial velocity around  $v_{\text{hel}} = 332$  km s<sup>-1</sup>. Therefore, the distance and velocity of this BHB star both suggest an association with the LMC. It lies about  $18^\circ$  from the center of the LMC, making it one of the



LMC’s most distant spectroscopically confirmed BHB members. Clearly, finding additional LMC stars with similar radial velocity at separate positions on the sky would help our understanding of the structure and dynamics of the LMC’s outer regions.

### 3.2.2. RR Lyrae Stars

Car II contains 3 RR Lyrae stars (Paper I). Our spectroscopic runs targeted 2 of those stars, namely MAGLITES J073637.00–580114.5 and MAGLITES J073645.86–575154.1 (or V1 and V2 in Paper I), which are the two innermost of the RR Lyrae stars, with distances from the center of Car II of 2’1 and 7’7. The derivation of the center-of-mass velocity, or systemic velocity, of RR Lyraes requires special treatment since the radial velocity for these stars changes significantly (up to  $\sim 100$  km/s for RRAb stars) during their pulsation cycle. A model of a radial velocity curve must be fitted to the spectroscopic data. To do this, we followed the procedure developed in Vivas et al. (2008). The observational data and the fitted model for each star are shown in Figure 3. As the period of RR Lyrae is usually less than a day, we measured the velocities from the January 23 and January 25 AAT observations separately. For other measurements, we used the velocity measured over 1-3 combined exposures from that night, as reported in Table 4. We therefore have 5 independent velocity measurements for V1 and 3 for V2.

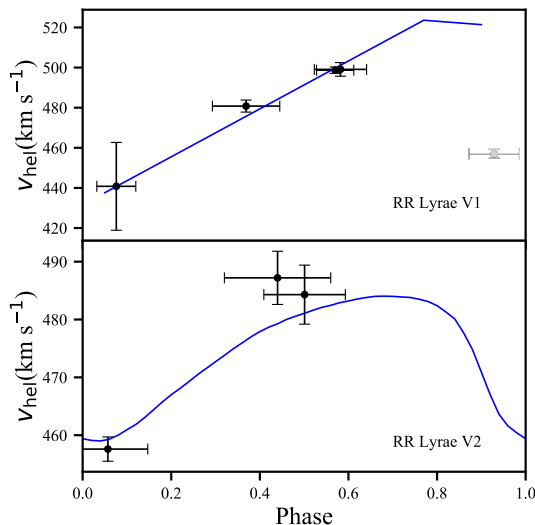


**Figure 3.** Radial velocity curve fits for the observations of the RR Lyrae stars MAGLITES J073637.00–580114.5 (V1, top) and MAGLITES J073645.86–575154.1 (V2, bottom). Circles represent the measurements from each individual spectrum, which were obtained at different phases during the pulsation cycle. The rightmost symbol (grey) for V1 (at phase 0.93) is shown only for reference but it was not used in the fitting of the radial velocity curve since it is located near a large discontinuity in the radial velocity curve. Error bars on the horizontal axis are not real errors but represent the time span (in units of phase) over which each spectrum was obtained. Solid lines represent the models fitted to both stars, X Ari in the case of the RRAb star V1, and a template based on T Sex and DH Peg in the case of the RRC star V2.

For V1, an RRAb star, we used the radial velocity model of the star X Arietis, which was parametrized

by Layden (1994) based on observations made by Oke (1966). The radial velocity curve of the ab-type RR Lyrae stars (the type of our star V1) has a large discontinuity near maximum light. Thus, it is advisable not to measure radial velocities near that phase in the pulsation cycle ( $\phi < 0.05$  or  $\phi > 0.9$ ). However, at the time of the spectroscopic observations we had not obtained final light curves of the RR Lyrae stars and thus, spectra were taken at random phases. Phases were calculated later once the light curves were characterized by Paper I. One of our observations for V1 was indeed not useful since the spectrum was acquired at phase  $\phi = 0.93$ . Thus, the radial velocity curve was fitted using 4 observations with phases ranging from 0.08 to 0.58. As seen in Figure 3, all the individual observations follow very nicely the model of X Arietis, which was shifted in velocity to match the observations. The best match was produced when the systemic velocity was  $491 \text{ km s}^{-1}$ . The rms of the fit is  $2.8 \text{ km s}^{-1}$ . However, to obtain a more realistic error we followed Vivas et al. (2005) and included uncertainties due to star-to-star variations of the amplitude of the radial velocity curve as well as possible differences on the exact phase of the systemic velocity. We determine a final systemic (heliocentric) velocity for V1 of  $491 \pm 7 \text{ km s}^{-1}$ .

For V2, which is an RRC star, we used a template constructed by Duffau et al. (2006) based on observations of T Sex and DH Peg. The amplitude of the radial velocity curve of RRC stars is not as large as for RRAb variables, nor is there a discontinuity at maximum light. Thus, all 3 spectra available for this star can be used to determine its velocity. We measure a heliocentric velocity for V2 of  $474 \pm 5 \text{ km s}^{-1}$ .

The systemic radial velocities obtained for these two RR Lyrae stars confirm that they are members of Car II.

### 3.3. Velocity Dispersion

We used 8 RGB stars (excluding the 2 binaries mentioned in § 3.2) and 6 BHB stars (hereafter the 14 star sample) to calculate the systemic velocity and the velocity dispersion of Car II using the 2-parameter Gaussian likelihood function defined in Walker et al. (2006) and an MCMC to sample the distributions of the systemic velocity  $v_{\text{hel}}$  and the velocity dispersion  $\sigma_v$ . We used a flat prior for the systemic velocity with range (455,495)  $\text{km s}^{-1}$  and a non-informative Jeffreys prior for the velocity dispersion with range (0.01, 100)  $\text{km s}^{-1}$  (or equivalent to a flat prior in  $\log(\sigma_v)$  space with range (-2, 2)). The probability distribution from the MCMC is shown in Figure 4. We find a systemic velocity of  $v_{\text{hel}} = 477.2 \pm 1.2 \text{ km s}^{-1}$  and a velocity dispersion of  $\sigma_v = 3.4^{+1.2}_{-0.8} \text{ km s}^{-1}$ , where we report the median of the posterior and the uncertainty calculated from the 16th and 84th percentiles.

In order to test the effects of our input assumptions, we also calculated the systemic velocity and velocity dispersion with different priors and different datasets. A summary of these comparisons is presented in Table 3. With a flat prior for velocity dispersion and the same 14 star sample, the velocity dispersion is  $3.8^{+1.3}_{-0.9} \text{ km s}^{-1}$ , which is slightly higher than the value determined using the Jeffreys prior with same dataset. This result is similar to what has been seen in Kim et al. (2015). If we

**Table 3**  
Systemic velocity and velocity dispersion with different datasets

Name	Dataset	prior	$v_{\text{hel}}$ ( $\text{km s}^{-1}$ )	$\sigma_v$ ( $\text{km s}^{-1}$ )
14 star sample (default)	8 RGB + 6 BHB	Jeffreys	$477.2 \pm 1.2$	$3.4^{+1.2}_{-0.8}$
14 star sample	8 RGB + 6 BHB	flat	$477.2 \pm 1.3$	$3.8^{+1.3}_{-0.9}$
16 star sample	8 RGB + 6 BHB + 2 RRL	Jeffreys	$477.4 \pm 1.2$	$3.5^{+1.2}_{-0.9}$
RGB only	8 RGB	Jeffreys	$476.6 \pm 1.2$	$3.5^{+1.3}_{-0.9}$
BHB only	6 BHB	Jeffreys	$478.8 \pm 2.2$	$0.9^{+3.7}_{-0.9}$
IMACS only	4 RGB	Jeffreys	$475.8 \pm 2.1$	$4.0^{+2.7}_{-1.7}$
VLT only	4 RGB + 2 BHB	Jeffreys	$477.1 \pm 1.5$	$3.3^{+1.7}_{-1.1}$
AAT only	5 BHB	Jeffreys	$480.9 \pm 2.5$	$0.2^{+2.4}_{-0.2}$
one-epoch	10 RGB (incl. 2 Binary) + 6 BHB	Jeffreys	$477.8 \pm 2.2$	$7.7^{+1.8}_{-1.4}$

**Note.** — All values reported here (and in this paper) are from the 50th percentile of the posterior probability distributions. The uncertainties are from the 16th and 84th percentiles of the posterior probability distributions.

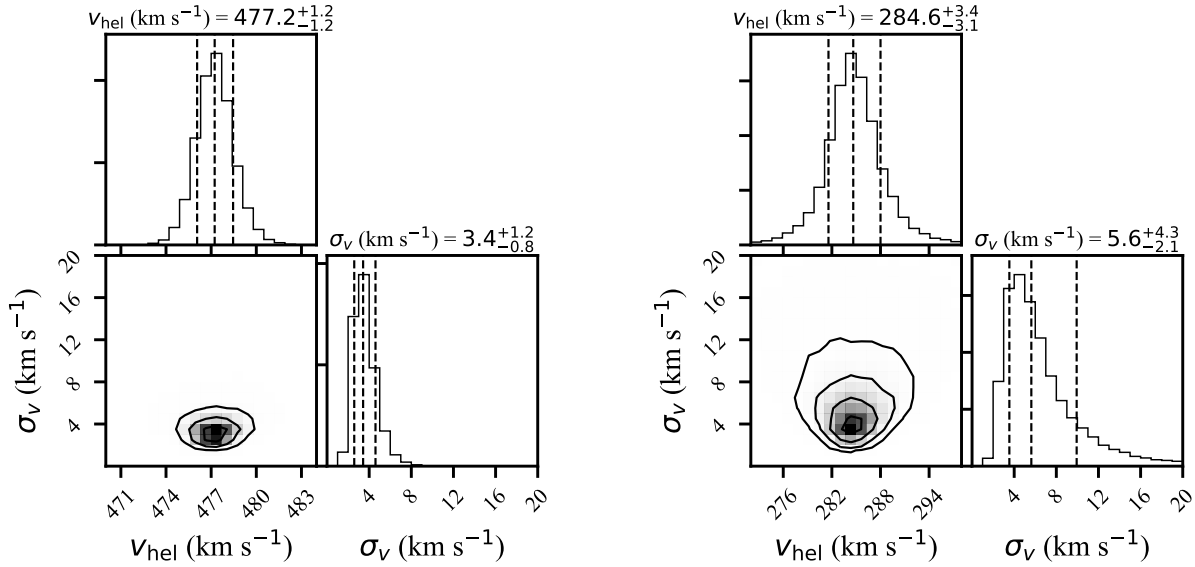


**Figure 4.** Two-dimensional and marginalized posterior probability distributions from an MCMC sampler using a likelihood model for the systemic velocity and velocity dispersion of Car II (*left*) and those of Car III (*right*). The 16th, 50th, and 84th percentiles are indicated by dashed lines in the 1-D histograms.

expand our sample to 16 stars by including the two RR Lyrae stars using the velocities derived in §3.2.2, both the systemic velocity and the velocity dispersion are very similar to what we determined with the 14 star sample (default sample). We then run similar calculations with only RGB members and only BHB members. The result with 8 RGB members is again very similar to our default sample, suggesting that the results are mostly constrained by the RGB members (which have smaller velocity uncertainties). The 6 BHB members give a smaller dispersion, but with larger uncertainties so that the results are statistically consistent, mainly due to the large velocity uncertainties ( $\delta_v \gtrsim 4 \text{ km s}^{-1}$ ) on the BHB stars.

We also calculated the systemic velocity and velocity dispersion using the results from each instrument to see if there is any instrumental bias. We obtain very consistent results using the VLT data or IMACS data alone, while the AAT data show much smaller dispersion as the members found by AAT are mostly BHBs (plus RR Lyraes and binaries). We additionally calculated the ve-

locity dispersion using the velocity measurements from only one epoch. We include the 14 stars in addition to the two binaries. For each star the measurement with highest S/N was chosen. The derived velocity dispersion is more than doubled compared to that derived from the 14 star sample. This exercise mimics a case in which only single-epoch velocity measurements are made for each star and therefore no binary information is available. Because of the large velocity amplitudes of the two binary stars, observations made near the velocity extrema of the binary orbits can substantially inflate the apparent velocity dispersion of Car II.

Finally, we performed a jackknife test (MacQueen 1967) to assess the robustness of the measured velocity dispersion with the 14 star sample, in particular, to check whether the results are driven by any single star. We remove one star out of the 14 star sample and recompute the average velocity and velocity dispersion. In the jackknife runs, the average velocity had a median difference of  $0.0 \text{ km s}^{-1}$ , a standard deviation of

0.3 km s<sup>-1</sup> and a minimum and maximum difference of -0.5 km s<sup>-1</sup> and 0.6 km s<sup>-1</sup>. For the velocity dispersion the median difference was 0.1 km s<sup>-1</sup>, the standard deviation 0.2 km s<sup>-1</sup>, and the minimum and maximum -0.5 km s<sup>-1</sup> and 0.3 km s<sup>-1</sup>. We conclude that, apart from the binaries, there are no individual stars whose inclusion or exclusion from the sample significantly affects the kinematics of Car II.

We checked if Car II contains a velocity gradient following the method in Li et al. (2017). We calculate a best-fit velocity gradient of  $0.0 \pm 0.3$  km s<sup>-1</sup> arcmin<sup>-1</sup>, consistent with the null model. We computed the Bayes Factor comparing the velocity gradient and constant velocity dispersion models and find  $\ln B = -2.2$ , which favors the constant velocity dispersion model (we follow Wheeler et al. 2017 to interpret the Bayes' Factor value). We conclude that there is no evidence for a velocity gradient in Car II.

For Car III, we determined a systemic velocity of  $284.6^{+3.4}_{-3.1}$  km s<sup>-1</sup> and velocity dispersion of  $5.6^{+4.3}_{-2.1}$  km s<sup>-1</sup> using the 4 identified members. We caution that the small number of stars may not lead to a reliable estimate for the velocity dispersion of Car III. Furthermore, a single binary star can easily inflate the velocity dispersion. We give a more detailed discussion of the implications of the measurements and the nature of Car III in §4.1.

#### 3.4. Metallicity and Metallicity Dispersion

We measured the metallicity of the red giant member stars in both systems using the equivalent widths (EWs) of the CaT lines. Following the procedure described by Simon et al. (2015) and Li et al. (2017), we fitted all three of the CaT lines with a Gaussian plus Lorentzian function and then converted the summed EWs of the three CaT lines to metallicity using the calibration relation from Carrera et al. (2013) with absolute  $V$  magnitude. We first performed the color-transformation from DES- $g$  and DES- $r$  to apparent  $V$  magnitude using Equation (5) in Bechtol et al. (2015) and then adopted distance moduli of  $(m - M) = 17.86$  for Car II members and  $(m - M) = 17.22$  for Car III members to calculate absolute magnitudes. The statistical uncertainties on the EWs are calculated from the Gaussian and Lorentzian fit. We added a systematic uncertainty of 0.2 Å (as determined in Li et al. 2017) in quadrature with the statistical uncertainties to obtain the final EW uncertainties. The metallicity uncertainties shown in Table 4 are dominated by the uncertainties on the CaT EWs, with small contributions from the uncertainties on the distances, the stellar photometry, and the uncertainties on the calibration parameters from Carrera et al. (2013).

Among the 10 confirmed spectroscopic RGB members in Car II, we successfully measured metallicities for 9 stars. The metallicities of the Car II members range from  $[\text{Fe}/\text{H}] = -2.7$  to  $[\text{Fe}/\text{H}] = -1.9$ . We used a Gaussian likelihood model as described above for the velocities to calculate the mean metallicity and metallicity dispersion of Car II. We find a mean metallicity of  $[\text{Fe}/\text{H}] = -2.44 \pm 0.09$ , with a dispersion of  $\sigma_{[\text{Fe}/\text{H}]} = 0.22^{+0.10}_{-0.07}$ . The probability distribution from the MCMC is shown in Figure 5.

For Car III, we measured the metallicity of the bright-

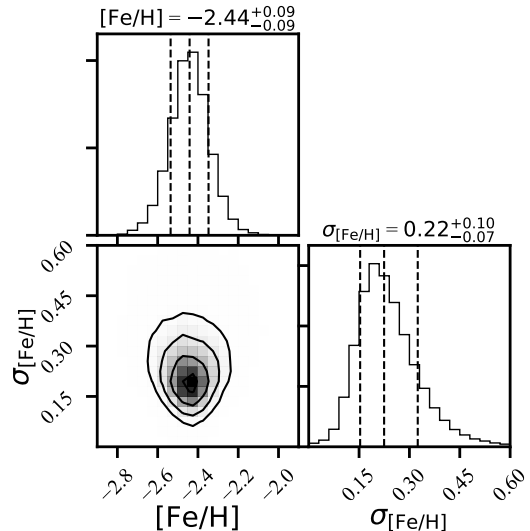


**Figure 5.** Two-dimensional and marginalized posterior probability distributions from an MCMC sampler using a likelihood model for the mean metallicity and metallicity dispersion of Car II. The 16th, 50th, and 84th percentiles are indicated by dashed lines in the 1-D histograms.

est RGB member, MAGLITES J073834.94-575705.4, and obtained  $[\text{Fe}/\text{H}] = -1.97 \pm 0.12$  for this star. If this RGB member represents the mean metallicity of Car III, then the metallicity of Car II and Car III are different at  $3\text{-}\sigma$  level. Note that in Paper I we obtained  $[\text{Fe}/\text{H}] = -1.8 \pm 0.1$  for Car II and  $[\text{Fe}/\text{H}] = -1.8 \pm 0.2$  for Car III from the isochrone fitting using photometry alone. While this metallicity estimate for Car III is consistent with that of the brightest RGB member from the spectroscopic measurements, for Car II the metallicity derived from isochrone fitting is more metal-rich than its spectroscopic mean metallicity.

## 4. DISCUSSION

### 4.1. Properties of Car II and Car III and Their Possible Association

We calculated the mass of Car II contained within the half-light radius according to the mass estimator from Wolf et al. (2010) (see also Walker et al. 2009b), using the velocity dispersion determined in §3.3 and the half-light radius of Car II from Paper I. We found a dynamical mass of  $M_{1/2} = 1.0^{+0.8}_{-0.4} \times 10^6 M_{\odot}$  and a mass-to-light ratio of  $369^{+309}_{-161} M_{\odot}/L_{\odot}$  for Car II. The reported uncertainties on the dynamical mass and mass-to-light ratio include the uncertainties on the velocity dispersion from this paper, and the uncertainties on the half-light radius and luminosity from Paper I. The mass of Car II is much larger than its stellar mass, and the mass-to-light ratio is similar to those of other dwarf galaxies with comparable luminosities. The low average metallicity ( $-2.44 \pm 0.09$ ) and large metallicity dispersion ( $0.22^{+0.10}_{-0.07}$ ) also match observations of other dwarf galaxies with similar luminosities (Kirby et al. 2013). We therefore conclude that Car II is a dark matter-dominated dwarf galaxy.

Because we have only identified 4 members of Car III, neither its mass nor its metallicity distribution is significantly constrained. We therefore cannot determine whether Car III is a dwarf galaxy. If the metallic-

ity of the brightest confirmed member star ( $[\text{Fe}/\text{H}] = -1.97$ ) represents the average metallicity of the system, then Car III is more metal-rich than most of the dwarf galaxies with similar luminosities, but still much more metal-poor than all known star clusters at a similar luminosity. If the velocity dispersion calculated from the 4 confirmed members is close to the true dispersion of the system, then Car III is likely to be a dark matter-dominated dwarf galaxy. Given the small sample, though, a single binary star could easily inflate the velocity dispersion, and therefore this dispersion shall be used with caution. Interestingly, among the 4 member stars, MAGLITES J073834.94–575705.4, the brightest RGB member, was observed in both January (IMACS) and February (VLT), and MAGLITES J073835.54–575622.3, a BHB member, was observed in January (IMACS), February (VLT) and May (AAT). The differences in velocities are consistent with the measurement uncertainties (see Table 4) and therefore we do not see any strong evidence for binarity of these two stars from our observations across 1-3 month baselines. However, the velocities of these two stars are about  $8 \text{ km s}^{-1}$  apart (and are the source of the large velocity dispersion on Car III). This large difference, if indeed not caused by binary motion, could provide a hint that Car III should be classified as a dwarf galaxy. Identifying more members with deeper observations will be necessary to confirm the nature of Car III. Observing these bright members at one or two additional epochs will also help determine whether or not they are in binary systems.

We note that the mass estimator from Wolf et al. (2010) is only valid for dispersion-supported stellar systems in dynamical equilibrium. It is possible that Car II has had a tidal interaction with the Milky Way ( $d \sim 36 \text{ kpc}$ ), LMC ( $d \sim 20 \text{ kpc}$ ), or Car III ( $d \sim 10 \text{ kpc}$ ) due to their close proximity. Either a velocity gradient or an increasing velocity dispersion at large radii could be potential signs of tidal disruption. In §3.3, we conclude that we are not able to detect a velocity gradient with our current data. In Figure 6, we show the velocity as a function of distance to the center of Car II. Interestingly, the six BHB stars are also the outermost members. As shown in Table 3, the velocity dispersion from the BHB sample alone is small due to the large velocity uncertainties, and therefore, we also do not see a larger velocity dispersion at large radii. However, we note that both null results could result from the large velocity uncertainties of these BHB stars. Further studies that either identify more RGB stars at large radii or improve the velocity precision for the known BHB members will be necessary to completely rule out a velocity gradient or other tidal effects.

The fact that all 6 BHB members are the outermost stars (Figure 6) implies a possible non-uniform spatial distribution of the stellar populations in Car II. However, we also caution that this distribution is likely caused by a selection bias from the observations. Note that the four outermost BHB members are uniquely identified by AAT, which has the largest FOV among three instruments. However, the target selection for AAT was performed with an older version of PARSEC isochrones and therefore may have missed a few RGB members with  $r > r_h$ , as explained in the Appendix. Further observations, including a more comprehensive search for bright

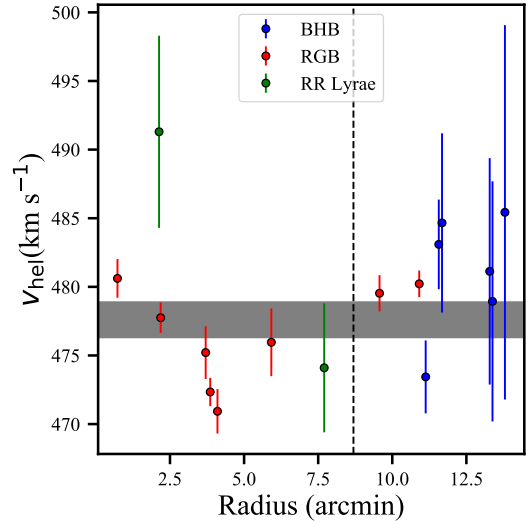


**Figure 6.** Velocity as a function of distance to the center of Car II, for Car II members only. Two binary stars are not shown. For the two RR Lyrae stars, the systemic velocities calculated in Sec 3.2.2 are used. The six outermost member stars are BHB members at  $r > 10'$ . The shaded region shows the systemic velocity of Car II with  $1 - \sigma$  uncertainty. The dashed line shows the half-light radius of Car II from Paper I.

RGB members outside of the half-light radius, may be necessary to fully understand the possible stellar population dependent spatial distribution in Car II.

To check whether the observed kinematics of Car II and Car III are consistent with their being gravitationally bound systems, we have computed their tidal radii ( $r_t$ ) with the Milky Way as the host via equation 18 in Bonivard et al. (2015b), using the Milky Way mass model presented in Eadie & Harris (2016). To set a lower limit on  $r_t$ , we used the Car II  $M_{1/2}$  value for the total mass and find  $r_t \sim 500 \text{ pc}$ . This lower limit on  $r_t$  is already significantly larger than the observed size of the system. With a mass profile based on a Navarro, Frenk, & White (1996) profile, the total mass of Car II (with  $r = 300 \text{ pc}$ ) is estimated to be 5 – 10 times larger than  $M_{1/2}$  (with  $r_s = 0.1 - 0.5 \text{ kpc}$ ), implying  $r_t \sim 0.9 - 1.1 \text{ kpc}$ . The mass profile of Car III is more uncertain due to the small number of stars and the unknown nature of the object. If we assume conservatively that Car III is a dwarf galaxy with dispersion  $\sigma = 1 \text{ km s}^{-1}$  and  $M(r_{\text{max}}) = 10 \times M_{1/2}$ , then we find  $r_t \sim 250 \text{ pc}$ , again much larger than the observed size of Car III. If the true dispersion of Car III is close to the measurement from a sample of 4 members, then the tidal radius will be even larger. We additionally computed  $r_t$  assuming that the LMC is the host instead of the Milky Way. For Car II, the LMC host  $r_t$  values are 5-10% larger than the Milky Way host values while for Car III they are  $\sim 50\%$  larger. Although a complete analysis of the Car II tidal radius should include the LMC+Milky Way system, we still expect the tidal radius to be larger than the observed size of Car II. Therefore, we conclude that Car II is likely to be a bound system based on its current location in the Milky Way, though it is still possible that it had a smaller tidal radius if it approached closer to the Milky Way or LMC in the past.

The small projected separation ( $\sim 18'$ ) of Car II and Car III and their similar distances naturally lead to the

question of whether the two are (or were) a bound pair of satellites. Similar speculation has occurred for the satellite pairs Leo IV–Leo V ( $\Delta d_{3D} \sim 20.6$  kpc and  $\Delta v \sim 47$  km s<sup>-1</sup>; Belokurov et al. 2008; Walker et al. 2009a; de Jong et al. 2010) and Pisces II–Pegasus III ( $\Delta d_{3D} \sim 43$  kpc and  $\Delta v \sim 10$  km s<sup>-1</sup>; Kim et al. 2015, 2016). While Car II and Car III have the smallest known physical separation to date,  $\Delta d_{3D} \sim 10$  kpc, their separation in velocity is quite large  $\Delta v \sim 193$  km s<sup>-1</sup>.

We applied the method presented in Evslin (2014) to estimate the minimum halo mass for the Car II–Car III system to be bound and find an unrealistically large halo mass of  $\sim 10^{11} M_{\odot}$  (similar to the halo mass of the LMC; van der Marel & Kallivayalil 2014). Based on the observed kinematics of Car II, the escape velocity at the distance of Car III is between 15 – 25 km s<sup>-1</sup>, significantly smaller than the observed velocity difference. Car II and Car III are therefore highly unlikely to be a bound pair of satellites.

Assuming the pair have similar proper motions, the two satellites would have had a close encounter and sailed past one another  $\sim 53$  Myr ago. Based on this trajectory and the observed separation they would have passed within 200 pc of one another ( $\sim 2 \times (r_{1/2, \text{Car II}} + r_{1/2, \text{Car III}})$ ). At the point of closest encounter, the Car III tidal radius would have been no more than a few tens of parsecs. Regardless of the nature of Car III, a close encounter between the satellites could have disrupted Car III. While there is no reason to expect Car II and Car III to have similar proper motions given the large difference in their radial velocities, it will be interesting to explore this scenario further when proper motions are available. We note that the brightest spectroscopic members in both Car II and Car III are brighter than the faint limit for Gaia proper motion measurements.

The properties of Car II and Car III derived in this paper are summarized in Table 2.

#### 4.2. Association with the Magellanic Clouds

As discussed in §1, the MagLiteS survey was designed to search for satellites of the Magellanic Clouds. Having searched in the vicinity of the LMC and SMC, it is therefore unsurprising that Car II and Car III are physically close to the Magellanic Clouds. The newly measured velocities of the Carina pair can now be used to test whether a physical association with the Clouds is likely.

To aid comparison with models, we first transform the line-of-sight velocities of Car II and Car III from the heliocentric frame to the Galactic Standard of Rest frame<sup>37</sup> (GSR) and obtain  $v_{\text{GSR, Car II}} = 235$  km s<sup>-1</sup> and  $v_{\text{GSR, Car III}} = 42$  km s<sup>-1</sup>. Next, we compare these measurements with the dynamical model of Magellanic satellites presented in Jethwa et al. (2016). Assuming an association with the LMC, this model predicts a velocity of  $v_{\text{GSR}} = 118_{-80}^{+142}$  (149<sup>+142</sup><sub>-114</sub> km s<sup>-1</sup>) at the position of Car II (Car III). For an association with the SMC, the predicted velocities are higher, at  $v_{\text{GSR}} = 350_{-70}^{+50}$  km s<sup>-1</sup>

<sup>37</sup> We adopted the circular orbital velocity of Milky Way at the Sun’s radius  $\Theta_0 = 239$  km s<sup>-1</sup> (McMillan 2011) and solar motion of  $(U_{\odot}, V_{\odot}, W_{\odot}) = (11.1, 12.24, 7.25)$  km s<sup>-1</sup> (Schönrich et al. 2010) for the velocity transformation from heliocentric to Galactic Standard of Rest to match the values used in Jethwa et al. (2016).

for both Car II and Car III. According to this model, both Carinas therefore have velocities consistent with an LMC association. In Figure 7, we show the comparison between the observed phase-space distribution of dwarf galaxies/dwarf galaxy candidates and the simulated probability distribution of LMC satellites from the Jethwa et al. (2016) model, and the neutral hydrogen gas column density from Nidever et al. (2010). According to the Jethwa et al. model, both Car II and Car III are consistent with having originated with the LMC.

As pointed out in §3.2.1, the non-rotating LMC halo population and the LMC rotating disk both have  $v_{\text{hel}} \sim 380$  km s<sup>-1</sup> at the location of Car II and Car III, which differs by  $\sim 100$  km s<sup>-1</sup> from the heliocentric velocities of Car II and Car III. According to van der Marel & Kallivayalil (2014), the enclosed LMC mass out to a radius of 8.7 kpc is  $M(< 8.7 \text{ kpc}) = 1.7 \times 10^{10} M_{\odot}$ . The corresponding escape velocity is  $\sim 90$  km s<sup>-1</sup> at the distance of Car II ( $\sim 18$  kpc from LMC) and  $\sim 75$  km s<sup>-1</sup> at the distance of Car III ( $\sim 25$  kpc from LMC). Because these values are based on a lower limit to the enclosed mass of the LMC, the actual escape velocities are likely to be somewhat larger. Therefore, we tentatively suggest that one or both of Car II and Car III are likely to be bound satellites of the LMC, although proper motion measurements will be needed to confirm this hypothesis.

We also note that all three newly discovered MagLiteS satellite candidates (Car II, Car III, and Pictor II) fall along a linear sequence on the sky as defined by the positions of the LMC, SMC and 7 of the DES satellite candidates. This configuration is shown by the dashed black line in Figure 7. This linear sequence was first pointed out in Jethwa et al. (2016), prior to any MagLiteS discoveries. As discussed in Paper I, it is unclear whether this linear sequence corresponds to a planar distribution of satellites around the Magellanic Clouds, or simply a satellite distribution that is elongated along the LMC–SMC separation vector. Once dynamical models of both scenarios are available, the velocities we have measured may provide a useful discriminant.

#### 4.3. J and D-factors

Milky Way satellite galaxies are among the most promising targets for indirect dark matter searches due to their substantial dark matter content, proximity, and dearth of conventional non-thermal emission (e.g., Baltz et al. 2008; Winter et al. 2016). In particular, analyses of  $\gamma$ -ray data from the *Fermi* Large Area Telescope (LAT) around previously known Milky Way satellites are now sensitive to dark matter annihilating at the canonical thermal relic cross section for particle masses up to 100 GeV (e.g., Ackermann et al. 2015; Geringer-Sameth et al. 2015). The discovery of additional Milky Way satellites, especially nearby objects such as Car II and Car III, can improve the sensitivity of such searches (He et al. 2015; Charles et al. 2016), as demonstrated by Drlica-Wagner et al. (2015b) and Albert et al. (2017).

In this subsection, we compute the astrophysical component of the dark matter annihilation and decay fluxes, the so-called J and D-Factors, for both Car II and Car III. The J-factor is the line-of-sight integral of the dark matter density squared:  $J(\theta) = \int \rho_{\text{DM}}^2 d\Omega dl$ . The D-Factor is the linear analog:  $D(\theta) = \int \rho_{\text{DM}} d\Omega dl$ . Here,  $\rho_{\text{DM}}$  is the



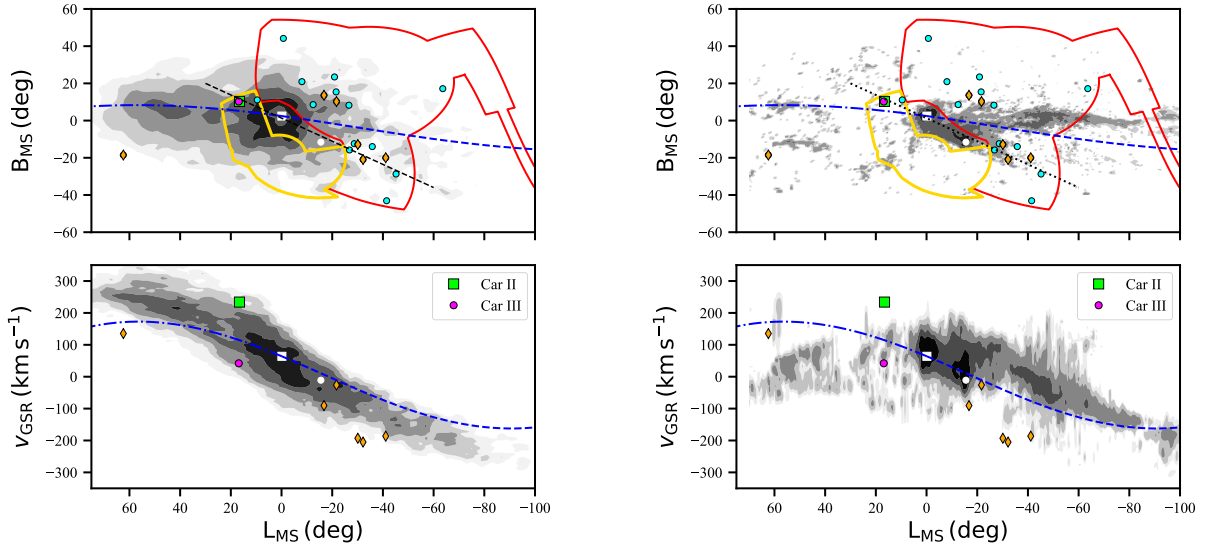


**Figure 7.** *Upper panels:* On-sky positions of the newly discovered satellites in DES (red outline) and MagLiteS (yellow outline), together with the LMC (white square) and SMC (white circle), shown in Magellanic Stream coordinates (Nidever et al. 2008). Car II and Car III, the Magellanic Clouds, and several other dwarf galaxies form a tight sequence on the sky. The black dashed line is a fit to this sequence as indicated in Paper I. *Lower panels:* Line-of-sight velocities for ultra-faint satellites near the Magellanic Clouds as a function of Magellanic Stream longitude. Objects with velocities from the literature are plotted as orange diamonds (Kirby et al. 2015b; Simon et al. 2015; Koposov et al. 2015; Walker et al. 2016; Simon et al. 2017), while measurements of Car II and Car III from this work are displayed in green and magenta, respectively. The gray contours show the probability distribution of the LMC satellites from Jethwa et al. (2016) (left) and the neutral hydrogen column density from Nidever et al. (2010) (right). The dash-dotted (dashed) curves show the leading (trailing) orbit of LMC.

dark matter density and the integral is performed over a solid angle  $\Delta\Omega$  with radius  $\theta$ . The standard approach for computing  $\rho_{\text{DM}}$  in dwarf spheroidal galaxies uses the spherical Jeans equation (e.g., Strigari et al. 2008a; Bonnavard et al. 2015a).

The three main ingredients of a spherical Jeans analysis are: the stellar density profile, which we modeled as a Plummer profile (Plummer 1911); the gravitational potential, assumed to be dark matter-dominated and modeled with a Navarro-Frenk-White profile (Navarro et al. 1996); and the stellar anisotropy, modeled with a constant profile<sup>38</sup>. Jeffreys priors are assumed for the dark matter halo parameters:  $-2 < \log_{10}(r_s/\text{kpc}) < 1$  and  $4 < \log_{10}(\rho_s/M_\odot \text{kpc}^{-3}) < 14$  for the scale radius,  $r_s$ , and scale density,  $\rho_s$ , respectively. Additionally, a prior of  $r_s > r_{1/2}$  is imposed, where  $r_{1/2}$  is the azimuthally averaged stellar half-light radius. We adopted the  $r_s > r_{1/2}$  prior for several reasons: in our posterior distributions there are no trends between  $J$  and  $r_s$  except for  $r_s < r_{1/2}$  where  $J$  is systematically higher, the  $J$ -factor tends to be overestimated in mock data sets without this cut (see Section 4.1 of Bonnavard et al. 2015a), and small  $r_s$  values are disfavored in  $\Lambda\text{CDM}$  N-body simulations (based on Garrison-Kimmel et al. 2014, a halo with  $V_{\text{max}} \sim 5 - 10 \text{ km s}^{-1}$  has a  $r_s \sim 100 - 300 \text{ pc}$ ). For the anisotropy prior, we assumed a flat symmetrized anisotropy parameter;  $-0.95 < \beta < 1.0$  (see Eq. 8 in Read et al. 2006). A flat prior was used for the average velocity ( $470 < \bar{v} < 490 \text{ km s}^{-1}$ ) and Gaussian priors were assumed for the distance and structural param-

eters<sup>39</sup>. We used an unbinned likelihood function (Strigari et al. 2008b; Martinez et al. 2009; Geringer-Sameth et al. 2015) and determined posterior distributions with the MultiNest sampling routine (Feroz & Hobson 2008; Feroz et al. 2009). We estimated the dark matter  $r_t$  (required to compute the J and D-Factors) at each point in the posterior distribution by iteratively computing the enclosed mass and solving for  $r_t$  as described in §4.1. We find the Car II  $r_t$  posterior to be roughly Gaussian, centered at 1 kpc but containing a substantial tail to larger values.

We calculated the Car II integrated J-factor enclosed within solid angles of radii  $\theta = \alpha_c, 0.1, 0.2, 0.5^\circ$  to be  $\log_{10}(J/\text{GeV}^2 \text{cm}^{-5}) = 18.1^{+0.5}_{-0.5}, 17.9^{+0.6}_{-0.5}, 18.0^{+0.5}_{-0.5}, 18.2^{+0.5}_{-0.5}$ , respectively, using the 14 star sample.  $\alpha_c$  is the angle within which the J-factor errors are minimized (Walker et al. 2011);  $\alpha_c = 2r_{1/2}/d \approx 0.23^\circ$  for Car II. The equivalent radius for the D-Factor occurs at  $\alpha_c/2$ . We determined the D-Factor within  $\theta = \alpha_c/2, 0.1, 0.2, 0.5^\circ$  to be  $\log_{10}(D/\text{GeV cm}^{-2}) = 17.1^{+0.3}_{-0.3}, 16.9^{+0.3}_{-0.3}, 17.4^{+0.3}_{-0.3}, 18.0^{+0.4}_{-0.4}$ . These values agree with the simple J-factor estimator (Eq. 13 of Evans et al. 2016). This value is an order of magnitude smaller than the simple empirical J-distance scaling relations (Drlica-Wagner et al. 2015b; Albert et al. 2017). The J-factor contains a large velocity dispersion scaling ( $J \propto M^2 \propto \sigma^4$ ) and an increase of only  $\Delta\sigma \sim 1.5 \text{ km s}^{-1}$  would move Car II onto the J-distance scaling relation (Pace & Strigari in prep). There are multiple ultra-faint

<sup>38</sup> Analysis with generalized stellar, dark matter, and anisotropy profiles would produce larger confidence intervals (Bonnivard et al. 2015b).

<sup>39</sup> We used the azimuthally averaged half-light radius to account for the axisymmetry of the systems ( $r_{1/2} = r_{\text{azimuthal}} = r_{\text{major}}\sqrt{1-\epsilon}$ ). For non-spherical analysis of dwarf galaxy J-factors see Hayashi et al. (2016) and Sanders et al. (2016).

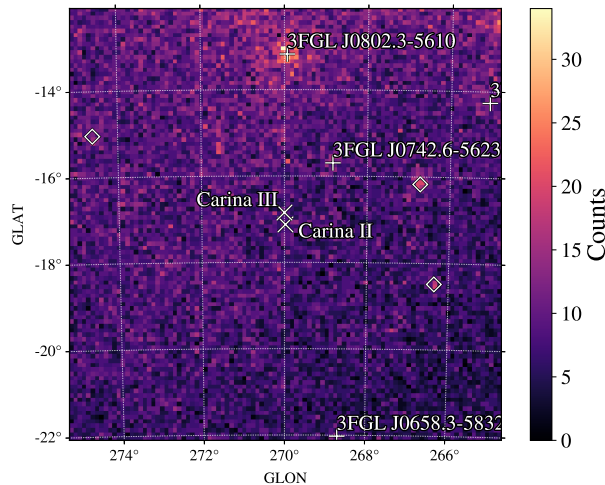


**Figure 8.** *Fermi* LAT  $\gamma$ -ray counts map ( $E > 1$  GeV) in the vicinity of Car II and Car III (Galactic coordinates). White plus signs indicate the positions of known gamma-ray sources from the 3FGL. Open diamonds indicate the positions of new gamma-ray point-source candidates found in this analysis.

satellites with larger J-factors (6 – 8 are larger depending on the J-factor compilation; Geringer-Sameth et al. 2015; Bonnivard et al. 2015b). The D-Factor at  $0.1^\circ$  is smaller than most of the other dSphs (Bonnivard et al. 2015b). Though Car II has similar distance and velocity dispersion to Ret II, its J-factor is smaller because it has a larger  $r_{1/2}$  (Pace & Strigari in prep). Car II is therefore not the most promising individual target for a dark matter annihilation signal but will be a useful addition in stacked analyses.

We applied the same methodology to the 4 star sample of Car III. We find the integrated J-factor within solid angles of radii  $\theta = \alpha_c, 0.1, 0.2, 0.5^\circ$  to be  $\log_{10}(J/\text{GeV}^2 \text{cm}^{-5}) = 19.8^{+1.0}_{-0.9}, 19.9^{+1.0}_{-0.9}, 20.1^{+1.0}_{-0.9}, 20.2^{+1.0}_{-0.9}$ , respectively.  $\alpha_c = 0.08^\circ$  for Car III. The D-Factor for Car III is  $\theta = \alpha_c/2, 0.1, 0.2, 0.5^\circ$  to be  $\log_{10}(D/\text{GeV cm}^{-2}) = 17.2^{+0.5}_{-0.4}, 17.8^{+0.5}_{-0.5}, 18.3^{+0.6}_{-0.5}, 18.8^{+0.6}_{-0.7}$ . The J-factor estimation of Car III is larger than Car II due to its proximity, smaller size, and larger (but uncertain) velocity dispersion. From our analysis, Car III potentially has one of the largest J-factors. However, given the very small stellar kinematic sample and the uncertain classification of Car III, it is premature to draw strong conclusions about the suitability of Car III as a dark matter annihilation target. As discussed in §4.1, the large velocity dispersion could result from binary star motions, small number statistics, or possible tidal effects. As a cautionary case in point, the Triangulum II ultra-faint dwarf galaxy has recently had its J-Factor values revised downward due to the identification of previously unsolved binary stars (Genina & Fairbairn 2016; Kirby et al. 2017). In addition, the velocity dispersion of Boötes II is likely overestimated in past determinations due to the presence of one binary star (Koch et al. 2009; Ji et al. 2016).

#### 4.4. Gamma-Ray Observations

We searched for excess  $\gamma$ -ray emission coincident with Car II and Car III using eight years of LAT data (2008 August 4 to 2016 August 5) passing the P8R2\_SOURCE event class selection from 500 MeV to 500 GeV. The low-energy bound of 500 MeV was selected to mitigate the impact of leakage from the bright limb of the Earth because the LAT point spread function broadens considerably below that energy. The high-energy bound of 500 GeV is chosen to mitigate the effect of the increasing residual charged-particle background at higher energies (Ackermann et al. 2015). To remove  $\gamma$  rays produced by cosmic-ray interactions in the Earth’s limb, we rejected events with zenith angles greater than  $100^\circ$ . To analyze data coincident with Car II and Car III, we used  $10^\circ \times 10^\circ$  regions of interest (ROIs) centered on each object. Data reduction was performed using *ScienceTools* version 11-05-03.<sup>40</sup>

We used the maximum-likelihood analysis pipeline described by Ackermann et al. (2014) to test for  $\gamma$ -ray emission coincident with Car II and III in excess of the known astrophysical backgrounds. The background model for the ROI includes Galactic interstellar emission (Acero et al. 2016), isotropic emission<sup>41</sup>, and point sources from a catalog derived from four years of data (3FGL; Acero et al. 2015). Car II and Car III reside in a region of the sky where the diffuse  $\gamma$ -ray background is relatively smooth (Galactic latitude of  $\sim 15^\circ$ ), and the nearest 3FGL catalog source is  $\sim 2^\circ$  away.

We first created a detection significance map for the entire  $10^\circ \times 10^\circ$  ROI by rastering a putative point source with fixed power-law spectrum ( $dN/dE \sim E^{-2}$ ) across the ROI in  $0.1^\circ$  steps and computing the improvement in the delta log-likelihood test statistic (TS; Mattox et al. 1996). This procedure led to the identification of three additional point-like source candidates in the region, none of which are within  $3^\circ$  of Car II or III (Figure 8). The TS obtained at the locations of Car II and Car III is 0.16 and 4.2, respectively, both consistent with the background-only hypothesis. We note that Car II and Car III would not be resolvable as independent sources given the resolution of the LAT instrument, which is  $\sim 1$  deg at 1 GeV and asymptotes to  $\sim 0.1$  deg above 10 GeV. The TSs associated with Car II and Car III are thus correlated, and can be attributed to a single excess of counts located  $\sim 0.7^\circ$  from Car III at  $(\alpha, \delta) = (114.5^\circ, -57.9^\circ)$ .

To search for  $\gamma$ -ray emission consistent with the annihilation of a dark matter particle into standard model products, we fit the  $\gamma$ -ray data coincident with Car II and Car III using a variety of spectral models generated by DMFit (Jeltema & Profumo 2008; Ackermann et al. 2014). We scan a range of dark matter masses spanning from 2 GeV to 10 TeV and annihilating through the  $b\bar{b}$  and  $\tau^+\tau^-$  channels. The most significant excess has TS = 6.2 and occurs for a dark matter particle with mass 35.4 GeV annihilating through the  $\tau^+\tau^-$  channel. Given that the statistical significance of this excess is well below the typical point-source detection criteria of the LAT (TS = 25), we calculate limits on the dark matter anni-

<sup>40</sup> <http://fermi.gsfc.nasa.gov/ssc/data/analysis/software/>

<sup>41</sup> <http://fermi.gsfc.nasa.gov/ssc/data/access/lat/BackgroundModels.html>

hilation cross section,  $\langle\sigma v\rangle$ , using the J-factors derived in §4.3. We find that Car II (Car III) can be used to constrain  $\langle\sigma v\rangle < 2.2 \times 10^{-24} \text{ cm}^3 \text{ s}^{-1}$  ( $3.3 \times 10^{-25} \text{ cm}^3 \text{ s}^{-1}$ ) for 100 GeV dark matter particles annihilating through the  $b\bar{b}$  channel. These constraints are  $\sim 100$  ( $\sim 10$ ) times larger than the thermal-relic cross section (i.e., Steigman et al. 2012). We again caution against overinterpreting the constraints derived from Car III because the J-factor value of Car III is derived from a very small stellar kinematic sample.

## 5. SUMMARY

In this paper, we presented the first spectroscopic analysis of the Carina II and Carina III dwarf galaxy candidates recently discovered in MagLiteS. Based on the kinematic and chemical properties of 18 confirmed spectroscopic member stars in Car II, we conclude that it is a dark-matter-dominated dwarf galaxy. On the other hand, only 4 members were identified in Car III. With this small spectroscopic sample we cannot yet determine whether Car III is a compact dwarf galaxy or an extended star cluster.

While Car II and Car III are located very close to each other both in sky projection ( $\sim 18'$ ) and in three dimensions ( $\sim 10 \text{ kpc}$ ), their systemic velocities differ by  $\sim 200 \text{ km s}^{-1}$ . We therefore conclude that these two systems are unlikely to be a pair of bound satellites.

Both Car II and Car III have line-of-sight velocities consistent with the hypothesis that they formed as members of a group of satellites around the Large Magellanic Cloud (LMC). Furthermore, one or both systems might remain bound to LMC due to the small difference in the line-of-sight velocity. The brightest RGB members in Car II and Car III are bright enough to have proper motion measurements from Gaia to test this hypothesis.

We further identify one blue horizontal branch (BHB) star as a likely LMC member in the region of Car II. Located at about  $18^\circ$  from the center of the LMC, this star is one of the LMC's most distant spectroscopically confirmed BHB members, and might provide hint on our understanding of the structure and dynamics of the LMC's outer regions.

No statistically significant excess of  $\gamma$ -ray emission is found at the locations of Car II and Car III in eight years of *Fermi*-LAT data. Using the J-factors derived from the kinematics data, Car II and Car III can be used to constrain the dark matter annihilation cross section.

TSL thanks Leo Girardi for helpful discussions regarding the PARSEC isochrones. The authors thank Louis Strigari for helpful conversations regarding the J-factor calculation. We are grateful for the service observations and Director's Discretionary time on AAT and VLT. We thank the service observers, Jeffrey Simpson and Chris Lidman, for collecting the AAT data during the service runs. We acknowledge the traditional owners of the land on which the AAT stands, the Gamilaraay people, and pay our respects to elders past and present.

This project is partially supported by the NASA Fermi Guest Investigator Program Cycle 9 No. 91201. JDS acknowledges support from the National Science Foundation under grant AST-1714873. ABP acknowledges generous support from the George P. and Cynthia Woods In-

stitute for Fundamental Physics and Astronomy at Texas A&M University. MASC is supported by the *Atracción de Talento* contract no. 2016-T1/TIC-1542 granted by the Comunidad de Madrid in Spain. APJ is supported by NASA through Hubble Fellowship grant HST-HF2-51393.001 awarded by the Space Telescope Science Institute, which is operated by the Association of Universities for Research in Astronomy, Inc., for NASA, under contract NAS5-26555. BCC acknowledges the support of the Australian Research Council through Discovery project DP150100862.

This research has made use of NASA's Astrophysics Data System Bibliographic Services. This research made use of *Astropy*, a community-developed core Python package for Astronomy (Astropy Collaboration et al. 2013). Contour plots were generated using *corner.py* (Foreman-Mackey 2016).

This project used data obtained with the Dark Energy Camera (DECam), which was constructed by the Dark Energy Survey (DES) collaboration. Funding for the DES Projects has been provided by the U.S. Department of Energy, the U.S. National Science Foundation, the Ministry of Science and Education of Spain, the Science and Technology Facilities Council of the United Kingdom, the Higher Education Funding Council for England, the National Center for Supercomputing Applications at the University of Illinois at Urbana-Champaign, the Kavli Institute of Cosmological Physics at the University of Chicago, the Center for Cosmology and Astro-Particle Physics at the Ohio State University, the Mitchell Institute for Fundamental Physics and Astronomy at Texas A&M University, Financiadora de Estudos e Projetos, Fundação Carlos Chagas Filho de Amparo à Pesquisa do Estado do Rio de Janeiro, Conselho Nacional de Desenvolvimento Científico e Tecnológico and the Ministério da Ciência, Tecnologia e Inovação, the Deutsche Forschungsgemeinschaft, and the Collaborating Institutions in the Dark Energy Survey. The Collaborating Institutions are Argonne National Laboratory, the University of California at Santa Cruz, the University of Cambridge, Centro de Investigaciones Energéticas, Medioambientales y Tecnológicas-Madrid, the University of Chicago, University College London, the DES-Brazil Consortium, the University of Edinburgh, the Eidgenössische Technische Hochschule (ETH) Zürich, Fermi National Accelerator Laboratory, the University of Illinois at Urbana-Champaign, the Institut de Ciències de l'Espai (IEEC/CSIC), the Institut de Física d'Altes Energies, Lawrence Berkeley National Laboratory, the Ludwig-Maximilians Universität München and the associated Excellence Cluster Universe, the University of Michigan, the National Optical Astronomy Observatory, the University of Nottingham, the Ohio State University, the OzDES Membership Consortium the University of Pennsylvania, the University of Portsmouth, SLAC National Accelerator Laboratory, Stanford University, the University of Sussex, and Texas A&M University.

Based on observations at Cerro Tololo Inter-American Observatory, National Optical Astronomy Observatory (NOAO Prop. ID 2016A-0366 and PI Keith Bechtol), which is operated by the Association of Universities for Research in Astronomy (AURA) under a cooperative agreement with the National Science Foundation.



*Facilities:* Magellan/Baade (IMACS); Very Large Telescope (GIRAFEE+FLAME); Anglo-Australian Telescope (AAOmega+2dF)

## REFERENCES

- Abbott, T., et al. 2005, arXiv:astro-ph/0510346
- Acero, F., et al. 2015, ApJS, 218, 23
- Acero, F., et al. 2016, Astrophys. J. Suppl., 223, 26
- Ackermann, M., et al. 2014, Phys. Rev. D, 89, 042001
- Ackermann, M., Albert, A., Anderson, B., et al. 2015, Physical Review Letters, 115, 231301
- Ackermann, M., et al. 2015, Astrophys. J., 799, 86
- Albert, A., Anderson, B., Bechtol, K., et al. 2017, ApJ, 834, 110
- An, D., Johnson, J. A., Clem, J. L., et al. 2008, ApJS, 179, 326
- Astropy Collaboration, Robitaille, T. P., Tollerud, E. J., et al. 2013, A&A, 558, A33
- Baltz, E., Berenji, B., Bertone, G., et al. 2008, J. Cosmology Astropart. Phys., 0807, 013
- Bechtol, K., Drlica-Wagner, A., Balbinot, E., et al. 2015, ApJ, 807, 50
- Belokurov, V., Erkal, D., Deason, A. J., et al. 2017, MNRAS, 466, 4711
- Belokurov, V., & Koposov, S. E. 2016, MNRAS, 456, 602
- Belokurov, V., Walker, M. G., Evans, N. W., et al. 2008, ApJ, 686, L83
- Besla, G., Martínez-Delgado, D., van der Marel, R. P., et al. 2016, ApJ, 825, 20
- Bonnivard, V., Combet, C., Maurin, D., & Walker, M. G. 2015a, MNRAS, 446, 3002
- Bonnivard, V., Combet, C., Daniel, M., et al. 2015b, MNRAS, 453, 849
- Boubert, D., Erkal, D., Evans, N. W., & Izzard, R. G. 2017, MNRAS, 469, 2151
- Bressan, A., Marigo, P., Girardi, L., et al. 2012, MNRAS, 427, 127
- Carrera, R., Pancino, E., Gallart, C., & del Pino, A. 2013, MNRAS, 434, 1681
- Charles, E., Sánchez-Conde, M., Anderson, B., et al. 2016, Physics Reports, 636, 1
- Cooper, M. C., Newman, J. A., Davis, M., Finkbeiner, D. P., & Gerke, B. F. 2012, spec2d: DEEP2 DEIMOS Spectral Pipeline, Astrophysics Source Code Library, ascl:1203.003
- de Jong, J. T. A., Martin, N. F., Rix, H.-W., et al. 2010, ApJ, 710, 1664
- Deason, A. J., Wetzel, A. R., Garrison-Kimmel, S., & Belokurov, V. 2015, MNRAS, 453, 3568
- D’Onghia, E., & Lake, G. 2008, ApJ, 686, L61
- Dooley, G. A., Peter, A. H. G., Carlin, J. L., et al. 2017, MNRAS, 472, 1060
- Dressler, A., Hare, T., Bigelow, B. C., & Osip, D. J. 2006, in Proc. SPIE, Vol. 6269, Society of Photo-Optical Instrumentation Engineers (SPIE) Conference Series, 62690F
- Dressler, A., Bigelow, B., Hare, T., et al. 2011, PASP, 123, 288
- Drlica-Wagner, A., Bechtol, K., Rykoff, E. S., et al. 2015a, ApJ, 813, 109
- Drlica-Wagner, A., Albert, A., Bechtol, K., et al. 2015b, ApJ, 809, L4
- Drlica-Wagner, A., Bechtol, K., Allam, S., et al. 2016, ApJ, 833, L5
- Duffau, S., Zinn, R., Vivas, A. K., et al. 2006, ApJ, 636, L97
- Eadie, G. M., & Harris, W. E. 2016, ApJ, 829, 108
- Evans, N. W., Sanders, J. L., & Geringer-Sameth, A. 2016, Phys. Rev. D, 93, 103512
- Evslin, J. 2014, MNRAS, 440, 1225
- Feroz, F., & Hobson, M. P. 2008, MNRAS, 384, 449
- Feroz, F., Hobson, M. P., & Bridges, M. 2009, MNRAS, 398, 1601
- Flaugher, B., Diehl, H. T., Honscheid, K., et al. 2015, AJ, 150, 150
- Foreman-Mackey, D. 2016, The Journal of Open Source Software, 24, doi:10.21105/joss.00024
- Garrison-Kimmel, S., Boylan-Kolchin, M., Bullock, J. S., & Kirby, E. N. 2014, MNRAS, 444, 222
- Genina, A., & Fairbairn, M. 2016, MNRAS, 463, 3630
- Geringer-Sameth, A., Koushiappas, S. M., & Walker, M. 2015, ApJ, 801, 74
- Geringer-Sameth, A., Koushiappas, S. M., & Walker, M. 2015, ApJ, 801, 74
- Geringer-Sameth, A., Walker, M. G., Koushiappas, S. M., et al. 2015, Physical Review Letters, 115, 081101
- Hayashi, K., Ichikawa, K., Matsumoto, S., et al. 2016, MNRAS, 461, 2914
- He, C., Bechtol, K., Hearin, A. P., & Hooper, D. 2015, Physical Review D, 91, 063515
- Jeltema, T. E., & Profumo, S. 2008, J. Cosmology Astropart. Phys., 11, 003
- Jethwa, P., Erkal, D., & Belokurov, V. 2016, MNRAS, 461, 2212
- Ji, A. P., Frebel, A., Simon, J. D., & Geha, M. 2016, ApJ, 817, 41
- Kim, D., Jerjen, H., Mackey, D., Da Costa, G. S., & Milone, A. P. 2015, ApJ, 804, L44
- Kim, D., Jerjen, H., Geha, M., et al. 2016, ApJ, 833, 16
- Kirby, E. N., Cohen, J. G., Guhathakurta, P., et al. 2013, ApJ, 779, 102
- Kirby, E. N., Cohen, J. G., Simon, J. D., & Guhathakurta, P. 2015a, ApJ, in press, arXiv:1510.03856
- Kirby, E. N., Cohen, J. G., Simon, J. D., et al. 2017, ApJ, 838, 83
- Kirby, E. N., Simon, J. D., & Cohen, J. G. 2015b, ApJ, 810, 56
- Koch, A., Wilkinson, M. I., Kleyna, J. T., et al. 2009, ApJ, 690, 453
- Koposov, S. E., Belokurov, V., Torrealba, G., & Evans, N. W. 2015, ApJ, 805, 130
- Layden, A. C. 1994, AJ, 108, 1016
- Li, T. S., Simon, J. D., Drlica-Wagner, A., & Bechtol, K. 2017, ApJ, 838, 8
- Mackey, A. D., Koposov, S. E., Erkal, D., et al. 2016, MNRAS, 459, 239
- MacQueen, J. 1967, in Proceedings of the Fifth Berkeley Symposium on Mathematical Statistics and Probability, Volume 1: Statistics (Berkeley, Calif.: University of California Press), 281–297
- Martinez, G. D., Bullock, J. S., Kaplinghat, M., Strigari, L. E., & Trotta, R. 2009, J. Cosmology Astropart. Phys., 6, 14
- Mattox, J., Bertsch, D., Chiang, J., et al. 1996, ApJ, 461, 396
- McMillan, P. J. 2011, MNRAS, 414, 2446
- Muñoz, R. R., Majewski, S. R., Zaggia, S., et al. 2006, ApJ, 649, 201
- Navarro, J. F., Frenk, C. S., & White, S. D. M. 1996, ApJ, 462, 563
- Nidever, D. L., Majewski, S. R., & Butler Burton, W. 2008, ApJ, 679, 432
- Nidever, D. L., Majewski, S. R., Butler Burton, W., & Nigra, L. 2010, ApJ, 723, 1618
- Nidever, D. L., Olsen, K., Walker, A. R., et al. 2017, ArXiv e-prints, arXiv:1701.00502
- Oemler, A., Clardy, K., Kelson, D., Walth, G., & Villanueva, E. 2017, COSMOS: Carnegie Observatories System for MultiObject Spectroscopy, Astrophysics Source Code Library, ascl:1705.001
- Oke, J. B. 1966, ApJ, 145, 468
- Pasquini, L., Avila, G., Allaert, E., et al. 2000, Proc. SPIE, 4008, 129
- Plummer, H. C. 1911, MNRAS, 71, 460
- Read, J. I., Wilkinson, M. I., Evans, N. W., Gilmore, G., & Kleyna, J. T. 2006, MNRAS, 367, 387
- Robin, A. C., Reylé, C., Derrière, S., & Picaud, S. 2003, A&A, 409, 523
- Sales, L. V., Navarro, J. F., Cooper, A. P., et al. 2011, MNRAS, 418, 648
- Sales, L. V., Navarro, J. F., Kallivayalil, N., & Frenk, C. S. 2017, MNRAS, 465, 1879
- Sanders, J. L., Evans, N. W., Geringer-Sameth, A., & Dehnen, W. 2016, Phys. Rev. D, 94, 063521
- Schlegel, D. J., Finkbeiner, D. P., & Davis, M. 1998, ApJ, 500, 525
- Schönrich, R., Binney, J., & Dehnen, W. 2010, MNRAS, 403, 1829
- Sharp, R., Saunders, W., Smith, G., et al. 2006, in Proc. SPIE, Vol. 6269, Society of Photo-Optical Instrumentation Engineers (SPIE) Conference Series, 62690G
- Simon, J. D., & Geha, M. 2007, ApJ, 670, 313
- Simon, J. D., Li, T. S., Drlica-Wagner, A., & Bechtol, K. 2017, ApJ, 838, 11

- Simon, J. D., Drlica-Wagner, A., Li, T. S., et al. 2015, *ApJ*, 808, 95
- Sohn, S. T., Majewski, S. R., Muñoz, R. R., et al. 2007, *ApJ*, 663, 960
- Steigman, G., Dasgupta, B., & Beacom, J. F. 2012, *Phys. Rev. D*, 86, 023506
- Strigari, L. E., Koushiappas, S. M., Bullock, J. S., et al. 2008a, *ApJ*, 678, 614
- . 2008b, *ApJ*, 678, 614
- Torrealba, G., Belokurov, V., Koposov, S. E., et al. 2018, *MNRAS*, arXiv:1801.07279
- van der Marel, R. P., Alves, D. R., Hardy, E., & Suntzeff, N. B. 2002, *AJ*, 124, 2639
- van der Marel, R. P., & Kallivayalil, N. 2014, *ApJ*, 781, 121
- van der Marel, R. P., Kallivayalil, N., & Besla, G. 2009, in *IAU Symposium*, Vol. 256, *The Magellanic System: Stars, Gas, and Galaxies*, ed. J. T. Van Loon & J. M. Oliveira, 81–92
- van der Marel, R. P., & Sahlmann, J. 2016, *ApJ*, 832, L23
- van Dokkum, P. G. 2001, *PASP*, 113, 1420
- Vivas, A. K., Jaffé, Y. L., Zinn, R., et al. 2008, *AJ*, 136, 1645
- Vivas, A. K., Zinn, R., & Gallart, C. 2005, *AJ*, 129, 189
- Walker, M. G., Belokurov, V., Evans, N. W., et al. 2009a, *ApJ*, 694, L144
- Walker, M. G., Combet, C., Hinton, J. A., Maurin, D., & Wilkinson, M. I. 2011, *ApJ*, 733, L46
- Walker, M. G., Mateo, M., Olszewski, E. W., et al. 2006, *AJ*, 131, 2114
- . 2009b, *ApJ*, 704, 1274
- . 2016, *ApJ*, 819, 53
- Wheeler, C., Pace, A. B., Bullock, J. S., et al. 2017, *MNRAS*, 465, 2420
- Winter, M., Zaharijas, G., Bechtol, K., & Vandebroucke, J. 2016, *ApJ*, 832, L6
- Wolf, J., Martinez, G. D., Bullock, J. S., et al. 2010, *MNRAS*, 406, 1220
- Yanny, B., Newberg, H. J., Johnson, J. A., et al. 2009, *ApJ*, 700, 1282
- Zacharias, N., Finch, C. T., Girard, T. M., et al. 2013, *AJ*, 145, 44

APPENDIX  
PARSEC ISOCHRONES

In the course of our spectroscopic follow-up campaign on DES ultra-faint satellites (Simon et al. 2015, 2017; Li et al. 2017), we noticed that the location of the confirmed spectroscopic members in color-magnitude diagrams was shifted with respect to the PARSEC isochrones of a metal-poor stellar population in the DECam system (see e.g., Figure 1 in Simon et al. 2017). In particular, the confirmed RGB members are found to have bluer colors than indicated by PARSEC isochrones. This offset is on the order of  $g - r \sim 0.05$  mag and could significantly affect the target selection of the candidate members for spectroscopic follow-up. For the IMACS observations presented in this paper, the target selection used criteria similar to those applied by Simon et al. (2017) and therefore the effect caused by this shift was minimal. However, for AAT observations, targets were selected to be near the PARSEC isochrone and therefore most of the RGB members were missed as a result of this color offset. We therefore manually shifted the isochrone bluer for the target selection of VLT observation, as described in §2.3.

This offset was only apparent when comparing confirmed members of ultra-faint dwarf galaxies discovered with DECam to the PARSEC isochrone generated in the DECam system. A similar offset is not observed for the ultra-faint dwarfs discovered in SDSS. After consultation with the Padova team, we learned that the PARSEC isochrones were computed using the filter transmission of DECam only. However, in order to compute precise synthetic magnitudes, one should also consider the CCD quantum efficiency (QE), Earth’s atmospheric transmission, and the mirror reflectivity, etc. A newer version of the PARSEC models for the DECam system was updated<sup>42</sup> on 2017 July 17 with the latest version of the system response of DECam<sup>43</sup>. A comparison of different versions of DECam throughput and the corresponding PARSEC isochrones are shown in Figure 9. With the corrected DECam system response, the confirmed spectroscopic members in Car II are much closer to the updated PARSEC isochrone. The remaining small offset might be caused by an overestimate of the interstellar extinction<sup>44</sup>.

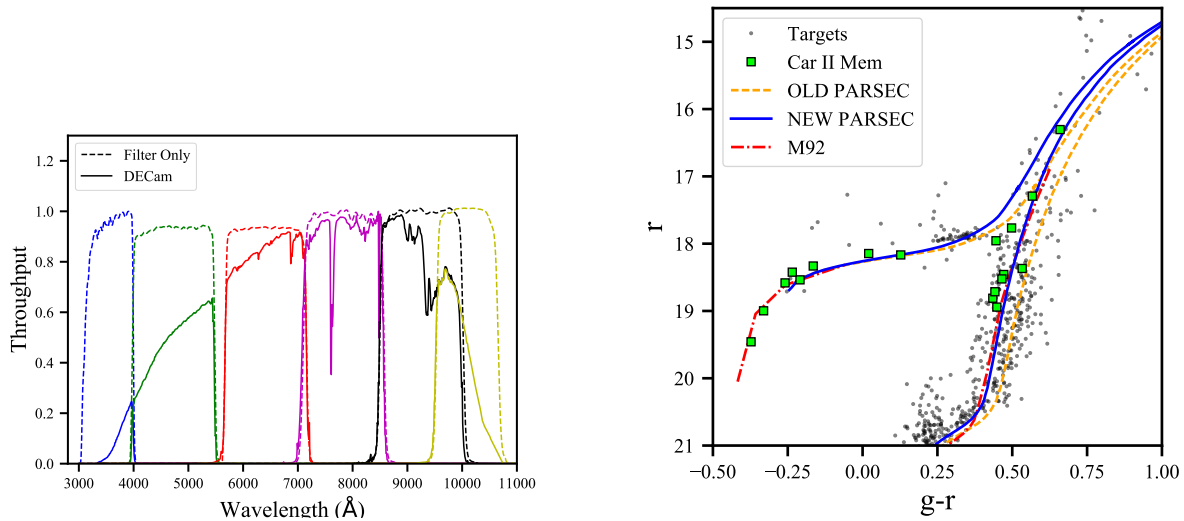


**Figure 9.** (left) A comparison of the DECam system throughput including filter response only (old) and combined (filter+CCD QE+atmosphere, new), both from CTIO website. (right) PARSEC isochrones of a metal-poor population with  $[\text{Fe}/\text{H}] = -2.2$ , age = 12 Gyr using the old and new DECam response. The new isochrone is well aligned with the confirmed members in Car II as well as the empirical isochrone of M92 from An et al. (2008) translated from SDSS to the DECam system (red dashed lines).

<sup>42</sup> PARSEC isochrones at <http://stev.oapd.inaf.it/cgi-bin/cmd>.

<sup>43</sup> Details of the DECam system response and filter throughput are available at CTIO website <http://www.ctio.noao.edu/noao/node/1033>. The specific system response file used to compute the new isochrones is available at <http://www.ctio.noao.edu/noao/>

[sites/default/files/DECam/DECam\\_filters.xlsx](sites/default/files/DECam/DECam_filters.xlsx).

<sup>44</sup> All photometry presented in this paper is corrected for interstellar extinction using the extinction map from Schlegel et al. (1998). The  $E(B-V)$  value around Car II and Car III is around 0.19

